Mapping 10-m global impervious surface area (GISA-10m) using multi-source geospatial data

Xin Huang[1,2], Jie Yang[1], Wenrui Wang[1], Zhengrong Liu[1]

[1] School of Remote Sensing and Information Engineering, Wuhan University, Wuhan, 430079, P.R. China
[2] State Key Laboratory of Information Engineering in Surveying, Mapping and Remote Sensing, Wuhan University, Wuhan, 430079, P.R. China

Correspondence to: Jie Yang (yang9tn@163.com)

Abstract. Artificial impervious surface area (ISA) documents the human footprint~~s~~. Accurate, timely, and detailed ISA datasets are therefore essential for global climate change studies and urban planning. However, due to the lack of sufficient training samples and operational mapping methods, global ISA datasets at a 10-m resolution are~~is~~ still lacking. To this end, we proposed a global ISA mapping method leveraging multi-source geospatial data. Based on the existing satellite-derived ISA maps and ~~the~~ crowdsourced~~ing~~ OpenStreetMap (OSM) data, 58 million training samples were extracted via a series of temporal, spatial, spectral, and geometric rules. We then produced a 10-m resolution global ISA dataset (GISA-10m) ~~Combined~~from ~~with~~ over 2.7 million Sentinel optical and radar images on the Google Earth Engine platform~~, we produced the 10-m global ISA dataset (GISA-10m)~~. Based on ~~the~~ test samples that are independent of~~to~~ the training set, GISA-10m ~~embraced~~ achieves an overall accuracy of greater than 86%. In addition, the GISA-10m dataset was comprehensively compared with the existing global ISA datasets, and the superiority of GISA-10m was confirmed~~demonstrated~~. The global road area was further ~~discussed~~ investigated, ~~by~~ courtesy of this 10-m dataset. It was found that China and the US~~nited States~~ ~~embraced~~ have the largest areas of ISA and road~~ area~~. The global rural ISA was found to be 2.2 times that of urban while the rural road area was found to be 1.5 times larger than that of the urban regions. The global road area accounts~~ed~~ for 14.2% of the global ISA, 57.9% of which is~~was~~ located in the top ten countries. Generally speaking, the produced GISA-10m dataset and the proposed sampling and mapping method are able to achieve rapid and efficient global mapping, and have the potential for detecting other land covers. It ~~was also indicated~~is also shown that global ISA mapping can be improved by incorporating OSM data. The GISA-10m dataset could~~an~~ be used as a fundamental parameter for Earth system science, and will provide valuable support for urban planning and water cycle study. The GISA-10m can be freely downloaded from http://doi.org/10.5281/zenodo.5791855 (Huang et al, 2021).

1 Introduction

The land dominated by humans has expanded rapidly over the past decades (Friedl et al., 2010), resulting in a large amount of terrestrial surface that is covered by impervious surfaces (Gong et al., 2020a). Impervious surfaces ~~ISA~~are ~~is~~ mainly composed of artificial materials, such as gravel, glass, asphalt, and metals (Tian et al., 2018). Such impervious surfaces~~ISA~~ prevent~~s~~ or decelerate~~s~~ water infiltration, while also blocking~~s~~ evapotranspiration, which affects the terrestrial water cycle and thermal environment (Qin et al., 2018; Yang et al., 2019). With more attention ~~attracted~~ now being paid to the impact of urban sprawl on the global climate environment (United Nations, 2016), the global monitoring of impervious surface area ~~(~~(ISA) ~~would~~can depict the anthropic implications on the water cycle, land cover, and biodiversity (Ji et al., 2020; Qin et al., 2017). In addition, ISA morphology is also an important parameter for urban planning, socio-economics, and population studies (Voss, 2007). In summary, accurate and timely monitoring of global ISA dynamics is ~~valuable~~ important for urban habitability (Herold et al., 2006), sustainable development (Dewan and Yamaguchi, 2009), and terrestrial ecosystem services (Goetz et al., 2003).

G~~The g~~lobal ISA monitoring via satellite remote sensing data has long been conducted~~recognized~~. Early efforts usually focused on global ISA mapping using coarse-resolution data, e.g., ~~DMSP (~~Defense Meteorological Satellite Program (DMSP) and ~~MODIS (~~Moderate Resolution Imaging Spectroradiometer (MODIS) data (Friedl et al., 2010; You et al., 2021). With the free availability of Landsat data and the advances in geospatial cloud platforms (e.g., Google Earth Engine, GEE), recent studies have focused on global annual ISA mapping at a 30~~-~~m resolution (Gong et al., 2020b; Gorelick et al., 2017; Liu et al., 2020c; Woodcock et al., 2008). For instance, Huang et al. ~~,~~(2021b) generated the ~~global~~ annual Global Impervious Surface Area (~~ISA dataset~~ GISA) dataset ~~(Global Impervious Surface Area) f~~covering~~rom~~ 1972 to 2019 using over three million Landsat images~~data~~. Although efforts have been ~~paid to the~~made in global ISA monitoring, few studies have focused on global ISA mapping at a 10-m resolution. Recently, Corbane et al.~~,~~ (2021) generated the Global Human Settlement Layer 2018 (GHSL 2018) dataset using Sentinel-2 composites and a convolutional neural ~~network~~network model~~s~~. However, GHSL 2018 focuses~~d~~ more on human settlements and lacks depiction of ISA, such as transportation facilities. In addition to these thematic datasets, ISA has~~was~~ also been documented in land~~-~~cover products. For example, Gong et al.~~,~~ (2019) ~~obtained~~ generated the~~a~~ ~~land cover map FROM_GLC10 (10-m~~ Finer Resolution Observation and Monitoring of Global Land Cover map~~)~~ for 2017 at a 10-m resolution (FROM_GLC10) using Sentinel-2 images. However, the accuracy of ISA in the land~~-~~cover datasets may not be sufficient to meet the needs of global climate change studies ~~studies~~ and urban planning ~~-~~(Gong et al., 2020b). Therefore, there is an urgent need for 10~~-~~m global ISA thematic datasets, ~~are in urgent need~~ to support various fine-scale applications.

Synthetic aperture radar (SAR) performs well in the case of ISA mapping due to its clear response to high-rise buildings and its ability to penetrate clouds (e.g., Sentinel~~-~~1) (Zhang et al., 2014). SAR data have the~~is~~ potential to~~for~~ reduce~~ing~~ the common false alarms that come~~derived~~ from ~~the~~ optical images, such as bare soil, but SAR systems ~~it~~ can be affected by complex terrain and shadows. Therefore, the existing studies ~~literatures~~ have investigated~~ed~~ the combination~~llaboration~~ of radar and optical data to improve ISA mapping. For example, Zhang et al.~~,~~ (2020) combined Landsat 8 and Sentinel-1 data to produce a 30-m global ISA dataset (the Global Land Cover with Fine Classification System, GLCFCS). Similarly, Marconcini et al.~~,~~ (2020) used Landsat ~~-~~8 and Sentinel-1 data to outline the world settlement footprint (World Settlement Footprint, WSF), based on support vector machine classifiers. Although the current studies have demonstrated the effectiveness of combining multi-source (e.g., radar and optical) remote sensing data for ISA mapping, they have usually focused on regional or national scales (Lin et al., 2020). In addition, combining data with different resolutions for ISA mapping can~~may~~ increase the uncertainty of the results. In particular, both Zhang et al.~~,~~ (2020) and Marconcini et al.~~,~~ (2020) generated global ISA (or settlement) datasets

~~by~~ using Landsat ~~-~~8 and Sentinel-1 data, but their resolutions were different, at 30 ~~-~~m~~m~~ and 10 ~~-~~m, respectively (Table 1). Generally speaking, 10-m global ISA mapping based on ~~the~~ multi-source remote sensing data (e.g., Sentinel-1 and 2) has~~ve~~ been insufficiently investigated in the current literature (Table 1).

Table 1. The existing global ISA datasets.

Name and abbreviation	Data and time span	Nominal resolution	Source of training sample	Classification method and strategy	Type d~~D~~efinition
Global Impervious Surface Area 30 m, *GISA* (Huang et al., 2021)	Landsat; 1972–~~—~~2019	30 ~~-~~m	MODIS land cover, Climate Change Initiative land cover, GHSL, FROM_GLC	Random forest classifier~~s~~ via hexagonal partitioning	Artificial impervious surface
Global Artificial Impervious Area, *GAIA* (Gong et al., 2020b)	Landsat; 1985–~~—~~2018	30 ~~-~~m	Visual interpretation	An exclusion-i~~I~~nclusion approach via 3.5° grid	Artificial impervious area
Global Annual Urban Dynamics, *GAUD* (Liu et al., 2020c)	Landsat; 1985–~~—~~2015	30 ~~-~~m	GAIA, GHSL, global urban land, global urban footprint	Random forest classifier~~s~~ via 1° grid; temporal segmentation	Urban extent
Global Human Settlement Layer 2018, *GHSL 2018* (Corbane et al., 2021)	Sentinel-2; 2018	10 ~~-~~m	Microsoft building footprint, Facebook settlement, European settlement map, GHSL	Convolutional neural network model~~s~~ within Universal Transverse Mercator zones	Human settlement
Finer Resolution Observation and Monitoring of Global Land Cover, *FROM_GLC 10* (Gong et al., 2019)	Sentinel-2; 2017	10 ~~-~~m	Visual interpretation	Random forest classifier~~s~~	Impervious surface
World Settlement Footprint, *WSF2015* (Marconcini et al., 2020)	Landsat ~~-~~8, Sentinel-1; 2015	10 ~~-~~m	Thresholding for spectral index, radar, and slope data	SVM classifier~~s~~ via 1° grid	Human settlement
Global Land Cover with Fine Classification System, *GLCFCS* (Zhang et al., 2020)	Landsat ~~-~~8, Sentinel-1; 2015	30 ~~-~~m	GlobeLand30	Random forest classifier~~s~~ via 5° grid	Impervious surface
Global Impervious Surface Area 10 ~~-~~m, *GISA-10m* (this study)	Sentinel-1, Sentinel-2; 2016	10 ~~-~~m	GISA, OSM GlobeLand30, FROM_GLC10	Random forest classifier~~s~~ via hexagonal partitioning	Artificial impervious surface

From the perspective of the global ISA mapping methods, supervised classification has been widely employed (Table 1). The quality of the training samples is the major factor affecting the classification results (Foody, 2009). Visual interpretation and automatic extraction from the existing datasets are two common ~~methods~~ ways to generate training samples. Visually-interpreted samples are usually accurate but ~~labour-intensive~~labor-intensive.~~.~~ T~~T~~herefore, they~~it~~ are~~is~~ often used for classification~~s~~ at a regional scale (Yang et al., 2020). On the other hand, samples generated from the existing datasets have been ~~proved~~ shown to be efficient for global ISA mapping in recent years (Marconcini et al., 2020; Zhang et al., 2020). In fact, ISA samples are typically diverse, as their response to the different sensors varies with the materials, geometry, atmospheric conditions, and viewing angles. Therefore, accurate and sufficient samples are required to address the above issue for the purpose of consistent ISA mapping at a~~the~~ global scale. Given the higher spatial resolution (10 ~~-~~m) of the Sentinel satellites, it remains challenging to obtain high-quality and adequate training samples for 10-m global ISA mapping.

In general, due to the difficulty of collecting training samples and the limitation of the computational and storage capacity required to deal with ~~the~~ massive data, efficient methods and accurate datasets ~~regarding~~ for 10-~~–~~m resolution global ISA mapping are lacking. Therefore, in this study, we proposed a global ISA mapping method that leverages multi-source geospatial data to map the~~ping~~ 10-m global impervious surface area (GISA-10m). To the best of our knowledge, this i~~wa~~s the first global 10-~~–~~m ISA map~~ping~~ based on ~~Sentienl~~Sentinel-1 and 2 data. Specifically, by combining ~~the~~ multi-source remote sensing data and ~~the~~ crowdsourced~~ing~~ OpenStreetMap data, we ~~proposed~~ developed a sample generation method involving a series of temporal, spatial, spectral, and geometric rules to collect training samples with a global coverage. ~~Besides~~Furthermore, an adaptive hexagonal partitioning strategy was ~~used~~ introduced for multi-source feature extraction and classification. Finally, the accuracy of the GISA-10m dataset was assessed using~~by~~ three independent sample sets. Meanwhile, we also compared ~~the~~ GISA-10m with the existing datasets, to better reflect its quality, and the ISA distribution in the global urban and rural regions was ~~analysed~~analyzed. In particular, the global road ISA was further extracted and ~~discussed~~investigated. Ablation experiments were also~~further~~ conducted to demonstrate the feasibility of OSM data in global ISA mapping.

2 Data

2.1 Remote sensing data

Sentinel-2 optical data and Sentinel-1 SAR data were used in the GISA-10m mapping. Sentinel-2 is a high-resolution multispectral imaging mission operated~~ing~~ by the European Space Agency (ESA) Copernicus program. The first Sentinel-2 satellite (Sentinel-2A) has been acquiring high-resolution Earth observation data since June 2015, consisting mainly of four 10-m resolution visible and near-infrared (NIR) bands, six 20-m resolution red-edge and short-wave~~wave~~ infrared (SWIR) bands, and three 60-m bands (Drusch et al., 2012; Zhang et al., 2018). After testing~~ed~~ and adjustment~~ed~~, a complete global coverage was obtained for the Sentinel-2 satellite in 2016 (Fig. S2). Therefore, we used all the available Level-1C top of atmosphere (TOA) reflectance data acquired in 2016 for the~~our~~ 10-m ISA mapping. S~~The s~~ystematic radiometric calibration and~~,~~ geometric and terrain correction have already been performed for the Level-1C TOA data by ~~the~~ ESA. Clouds and shadows were removed via the quality band to obtain cloud-free pixels.

The Sentinel-1A satellite was launched i~~o~~n April 2014, carrying a C-band SAR instrument~~synthetic aperture radar~~. After the launch of Sentinel-1B in 2016, the two satellites now have~~d~~ a return visit period of six days at the equator. We used all the available Ground Range Detected (GRD) images acquired under Interferometric Wide (IW) mode, with a spatial resolution of 10 ~~–~~m. The boundary noise removal, thermal noise removal, radiometric calibration, and terrain correction ~~has been~~were conducted on~~by~~ the GEE platform, with the same processing tools as the Sentinel-1 Toolbox. Sentinel-1 data in both ascending and descending orbit were considered. For the ~~places~~ locations where two orbits were available, only the descending data were~~as~~ used, to avoid the terrain distortion caused by the combination of two orbits (Veloso et al., 2017). In total, over 2.7 million Sentinel images were used to cover the global terrestrial surface (Fig. S2).

2.2 Volunteered geographic information data

Volunteered geographic information (VGI) is ~~the~~ geographic information that i~~wa~~s created, edited, and updated by volunteers (Goodchild, 2007). The well-known ~~VGI project,~~ OpenStreetMap (OSM) VGI project~~,~~ provides online maps that can be edited and used by everyone. Since its launch in 2004, OSM has been updated and maintained by over seven million volunteers (Haklay and Weber, 2008). OSM has been used for positioning and navigation (Fonte et al., 2020), urban modeling (Goetz, 2013), and land-cover mapping (Tian et al., 2019). In fact, over 600 million buildings and roads have~~were~~ been tagged in the OSM database (https://taginfo.openstreetmap.org/keys, last accessed: 17 Aug 2021). These data should be important reference data for ISA mapping~~,~~ but, unfortunately, in the current literature, they have seldom been used for ISA mapping at the global scale. Therefore, we used the OSM data as a source of ~~the~~ training samples for the GISA-10m mapping. Specifically, we extracted the buildings and road networks as potential training samples from the OSM P~~p~~lanet data built on January 2, 2017[1].

2.3 Existing ISA datasets

We ~~inter~~compared GISA-10m with the existing ISA datasets, i.e., ~~including~~ GISA, GAIA, GAUD, WSF2015, FROM_GLC10, GLCFCS, and ~~GHSL2018~~GHSL 2018 (Table 1). GISA, GAIA, and GAUD are Landsat-derived annual global ISA datasets for the time periods of 1972–~~-~~2019, 1985–~~-~~2018, and 1985–~~-~~2015, respectively. ~~GHSL2018~~GHSL 2018 is a global settlement layer based on a Sentinel-2 composite, where a convolutional neural network model was used to estimate the settlement probability (Corbane et al., 2021). WSF2015 and GLCFCS are global ISA datasets based on Landsat 8 and Sentinel-1 data. Marconcini et al. (2020) collected the samples for WSF2015 based on a set of spectral and topographic rules, and Zhang et al. (2020) derived the samples for GLCFCS from GlobeLand30. ~~WSF2015 collected samples based on a set of spectral and topographic rules, and GLCFCS derived samples from GlobeLand30 (Marconcini et al., 2020; Zhang et al., 2020)~~. Gong et al.~~,~~ (2019) generated the 10-m ~~global land cover product~~ FROM_GLC10 using Sentinel-2 data and random forest classifiers. It should be noted that these datasets ~~were~~ differ~~ent~~ ~~for~~in their mapping purposes and their ~~the~~ definitions~~s~~ of the land–~~-~~cover categories ~~and mapping purposes~~. For instance, ~~GHSL2018~~GHSL 2018 and WSF2015 focus~~ed~~ on human settlements, while GAUD delineates~~d~~ urban extent (Table 1). T~~In this study, ~~he GISA-10m dataset generated in this study ~~monitored~~reflects the ISA~~impervious surface area (ISA)~~ generated by human activities, including all kinds of human settlements, transportation facilities, industries, and mining locations~~places~~, ~~by~~ courtesy of the employment of the high spatial resolution satellite data. Therefore, artificial impervious surfaces and human settlements were treated as ISA in this ~~paper~~study.

[1] https://planet.openstreetmap.org/planet/2017/planet-170102.osm.bz2, last access: 13 Mar 2021

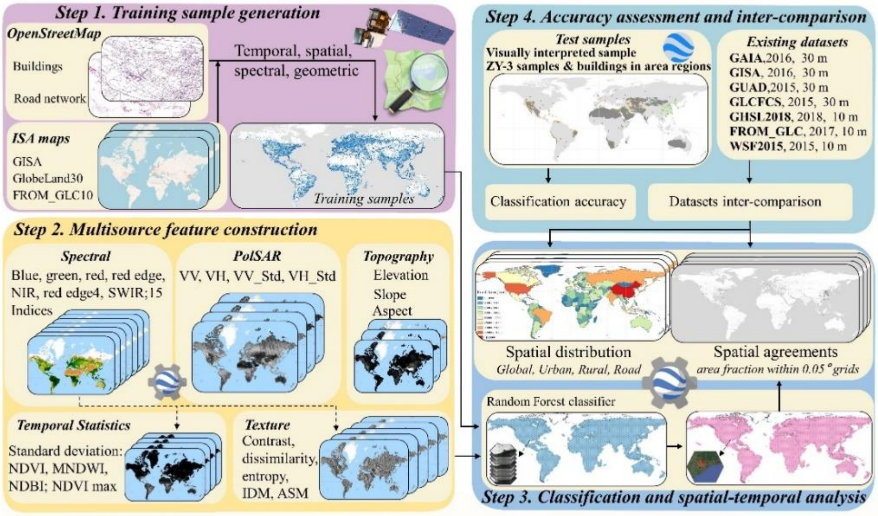

Figure 1. The flowchart for GISA-10m mapping.

3 Methodology

The main objectives of this study were to: 1) investigate ~~the~~ 10-m global ISA mapping (GISA-10m) by combining Sentinel-1 and -2 images with other geographic information; and 2) ~~analyse~~analyze the distribution of urban and rural ISA at a 10-m resolution. The flowchart for GISA-10m mapping i~~wa~~s shown in Fig. 1, including training sample generation, multi-source feature construction, ~~random forest~~ RF classification, accuracy validation, and dataset comparison. Based on the satellite-derived ISA maps and the VGI data (i.e., OpenStreetMap), we proposed a rule-based approach to automatically generate global training samples. Using more than 2.7 million Sentinel images on the GEE, multi-source features were ~~then~~ constructed and fed into the ~~random forest~~ RF classifier to obtain the mapping results. The accuracy of the GISA-10m was assessed by visual~~ly~~-interpretation~~ed~~ and ~~the~~ third-party samples. To better evaluate the performance of GISA-10m, we compared it with the current state-of-the-art global ISA datasets (Table 1). Finally, the distribution of ISA over urban and rural regions was ~~analysed~~analyzed.

3.1 Global ISA mapping using multi-source geospatial data

3.1.1 Sample collection

In the case of large-scale supervised classification, both the quantity and quality of samples are important (Foody and Arora, 1997). ISA is a highly variable object, and its attributes in the Sentinel-2 multispectral images are related to materials, viewing angles, and atmospheric conditions, while its response to the Sentinel-1 SAR instrument depends on dielectric properties, geometry, and surface roughness. Hence, a large number of training samples were required to address the afore-mentioned challenges that would be encountered at the global scale. Training samples a~~we~~re usually acquired by means of visual interpretation or automatic extraction from the existing datasets. However, t~~T~~he visual interpretation methods a~~we~~re ~~labour~~labor- and time-~~-~~intensive, even for small regions. Therefore, at a large scale, training samples a~~we~~re usually extracted from the existing datasets with similar temporal and spatial coverages. However, the sample quality i~~wa~~s affected by the quality of the datasets ~~used~~. Theoretically, samples extracted from a single dataset will~~may~~ result in more errors and uncertainties, while multi-source data~~sets~~ can improve the reliability of the training samples (Huang and Zhang, 2013). We therefore~~us~~ proposed to collect global training samples by incorporating the existing ISA datasets and the crowdsourced~~ing~~ OSM database. To ~~concisely~~ distinguish the two types of ISA samples, we named the ISA samples extracted from the existing satellite-derived ISA datasets as ISA_{RS} and those extracted from the OSM as ISA_{OSM}.

The existing ISA datasets generally cover~~ed~~ a broad terrestrial surface, but they ~~were~~ differ~~ent~~ in terms of their definitions~~s~~, spatial resolutions~~s~~, and temporal coverage. In this study, the GISA, FROM_GLC10, and GlobeLand30 products were chosen to extract the training samples, ~~due to~~for the following reasons: 1) the GISA is aimed at mapping the global ~~impervious surface area~~ISA, which ~~-w~~ias consistent with GISA-10m; 2) the team behind the GlobeLand30 employed extensive visual interpretation to detect artificial surfaces, which can effectively reduce the false alarms from other datasets, i.e., GISA and FROM_GLC10 (Chen et al., 2015); and 3) t~~T~~he definition of FROM_GLC10 (impervious surfaces) i~~wa~~s ~~also~~ consistent with that of GISA-10m, and its spatial resolution i~~wa~~s also 10 -m. The GHSL 2018, WSF2015, and GAUD were not considered since they aim~~ed~~ to outline human settlements or urban extent~~s~~ (Table 1). We then collected the eligible training samples according to the following rules.

(1) Temporal rule: The GISA i~~wa~~s a global ISA dataset covering~~during~~ 1972–2019, so~~and~~ we selected its results for~~of~~ 2016 to match the ~~time when~~ Sentinel data ~~was~~ used in this research. GlobeLand30 documents~~ed~~ global land cover ~~map~~ for 2000, 2010, and 2020, so~~and here,~~ the 2010 map was chosen in this study. Although the 2020 map i~~wa~~s more recent than the~~o~~ 2016 map, it contains~~ed~~ ISA that was built after 2016, making it unsuitable for the GISA-10m mapping. Although there is a six-year gap between GlobeLand30 and the other datasets (i.e., GISA and FROM_GLC10), ~~.~~ w~~W~~e adopted the commonly used assumption that the transition from ISA to non-impervious surface area (NISA) rarely happens~~ed~~ (Gong et al., 2020b; Huang et al., 2021, 2022), so that the GlobeLand30 for 2010 could~~an~~ be used for the GISA-10m mapping. The following spatial and spectral rules were used to remove the possible errors.

(2) Spatial rule: We first checked the class labels of the three datasets at each pixel. If these labels were the same (i.e., ISA), the pixel was taken as a potential ISA_{RS} sample. The incorporation~~collaboration~~ of multiple datasets can effectively reduce the errors that exist~~ed~~ in a single dataset. In addition, we filtered out the edge pixels in each dataset to reduce the uncertainty, since they were more likely to be mixed pixels. ~~-~~Edge pixels were defined as the outermost pixels of each ISA patch. We removed the edge pixels in each data~~-~~set, and then selected their ISA intersection as potential training samples. In this way, the errors contained in the non-edge pixels in the 30-m resolution data (e.g., mixed pixels) could~~an~~ be removed by the edge pixels in the 10-m resolution data.

(3) Spectral rule: After the above steps, ~~there may still be~~ a small amount of errors may still remain ~~-~~in the current samples. Hence, we applied the spectral rule to remove these erroneous samples. Specifically, we measured the

~~mahalanobis~~Mahalanobis distance between each ISA_{RS} sample to the spectral average of each hexagon (the mapping unit adopted in this study), and filtered out the samples with a distance greater than μ + δ (where μ and δ represent~~s~~ the mean and standard deviation, respectively) (Huang et al., 2021). Vegetation and water bodies a~~we~~re common sources of false alarms in the existing datasets (Fig~~s~~. 2a and ~~&~~b). However, these errors often account~~ed~~ for a relatively small proportion, and they can be effectively identified and reduced by the spectral rule. It can be seen in Fig. 2 that most of the water bodies and vegetation (~~e.g.~~the red rectangles in Fig. 2) were successfully removed from the initial ISA_{RS} training samples.

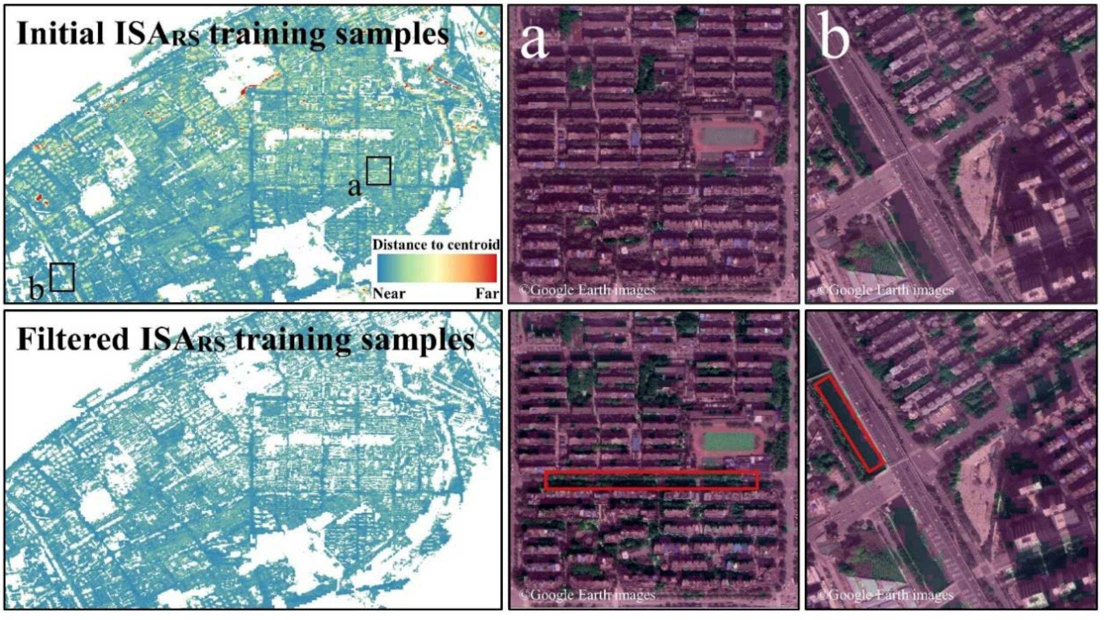

Figure 2. E~~The e~~xamples of the initial and filtered ISA_{RS} training samples from the city of~~in~~ Wuhan in China ~~city~~ (30.625382° N, 114.392682° E). The purple in the close-up maps represents the samples.

~~On the other hand,~~ W~~w~~e extracted the ISA_{OSM} samples from the OSM buildings and roads through the following rules.

(1) Temporal rule: We chose the OSM data built on ~~2~~ January 2, 2017, in terms of the time of GISA-10m. This version of the OSM data was employed to ensure that the buildings and roads were constructed in 2016 or before, and hence~~,~~ ~~it was~~were suitable for the 2016 ISA mapping.

(2) Geometric rule: A natural way to extract training points from OSM data i~~wa~~s to generate random points within the building or road polygons (Liu et al., 2020a). However, random points may contain erroneous or mixed pixels. Such problems can be mitigated by ~~making~~ applying negative buffers to the polygons (Liu et al., 2020a). However, this approach i~~wa~~s very time-consuming when applied to global ISA mapping, especially given the more than 200 million buildings in the OSM database. Therefore, in this study, we extracted the geometric center of a building polygon as an ISA_{OSM} sample, which was more efficient than buffering or~~and~~ random points. Notably, although we could~~an~~ filter out the erroneous buildings using attribute tags (e.g., dams, swimming pools, playgrounds), the geometric center of a building was not always an ISA sample. Hence, we further required that the geometric center must be contained by the building. As in Fig~~s~~. 3a and ~~&~~b, the incorrect building

geometric centers (e.g., the vegetation and water, as indicated by the yellow points) were successfully identified and removed by the geometric rule. In addition, we excluded buildings with an area of less than 100 ~~-~~m^2 (approximately~~∼~~ a Sentinel pixel), to ensure the reliability of the samples. This is b~~B~~ecause a~~the~~ training sample extracted from the geometric center may be NISA~~,~~ when the area of the~~a~~ building is smaller than a Sentinel pixel.

Compared with the widely used 30-m Landsat data, the high-resolution Sentinel data ~~promotes~~ allow a better delineation of roads. We thereby also extracted ISA$_{OSM}$ samples from the OSM road networks. The OSM roads usually consist~~ed~~ of centerlines rather than boundaries. Therefore, we extracted the center point of each road, rather than its geometric center, as the road ISA samples. Given that the width of low-grade roads may be ~~smaller~~ less than 10 ~~-~~m (i.e., a Sentinel pixel), we kept only the main roads (highway = “~~"~~primary”~~"~~).

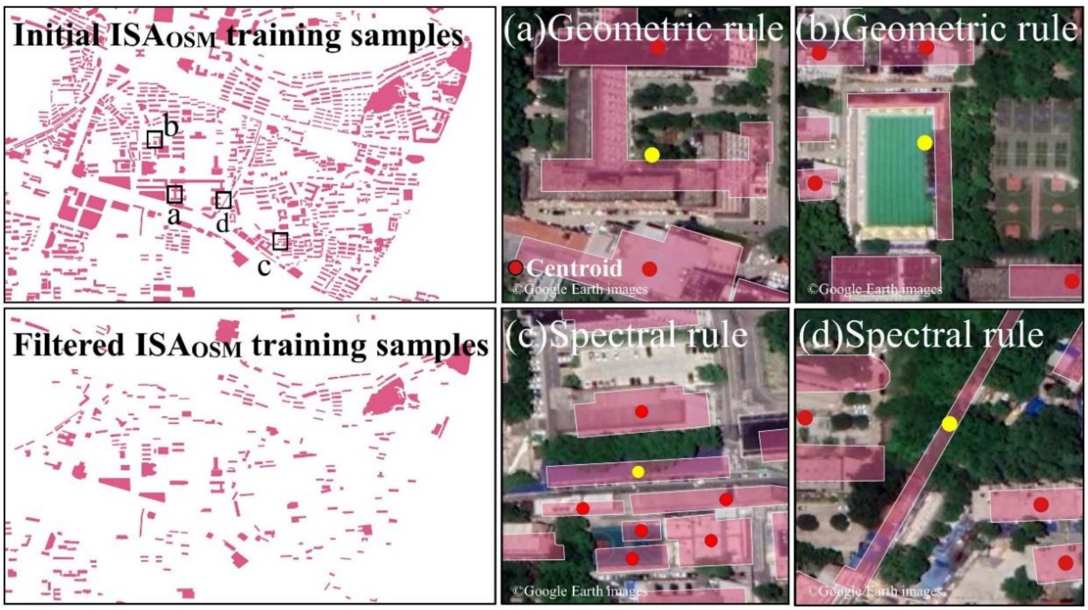

Figure 3. Examples of the initial and filtered ISA$_{OSM}$ training samples from the city of~~in~~ Wuhan in China ~~city~~ (30.530202° N, 114.356287° E). The yellow points in the close-up maps represent the errors recognized by (a)–(~~-~~b) the geometric rule and (c)–(~~-~~d) the spectral rule~~s~~.

(3) Spatial rule: Given the uneven spatial distribution of OSM data (Tian et al., 2019), we ~~then~~ applied the spatial rule to balance the~~its~~ distribution at the global scale. Specifically, for hexagons with more than 10,000 OSM records (i.e., buildings and roads), we randomly selected 10 ~~,~~000 records as initial samples. The dilution of OSM data can significantly reduce the subsequent computational cost. ~~In addition, considering that ISA$_{OSM}$ could overlie with ISA$_{RS}$, we removed the ISA$_{OSM}$ samples that were intersected with ISA$_{RS}$.~~ In the field of supervised classification, the diversity of the samples i~~wa~~s important for the generalization ability of the classification model (Huang and Zhang, 2013). Considering that ISA$_{OSM}$ can~~ould~~ overlie with ISA$_{RS}$, we removed the ISA$_{OSM}$ samples intersected with the ISA$_{RS}$ sample pool, to increase the diversity and reduce the redundancy of the ISA samples.

(4) Spectral rule: Although OSM uses humans as sensors, ISA$_{OSM}$ samples can~~may~~ still contain erroneous points, such as vegetation and water bodies,~~y~~ ~~beside~~ in addition to roads. As shown in Fig~~s~~. 3c and ~~&~~d, the yellow points satisfy~~ied~~ the temporal, spatial, and geometric rules, but they a~~we~~re actually vegetation. Hence, we applied the spectral rule to filter out these erroneous points~~m out~~. Specifically, the ISA$_{OSM}$ samples whose ~~MNDWI (~~modified normalized difference water index (MNDWI) or ~~NDVI (~~normalized difference vegetation index (NDVI)~~)~~ value was~~s~~ larger than $\mu+\delta$ were removed (μ and δ represent the mean and standard deviation of the indices, respectively), as these points were more likely to be vegetation or a water body (Huang et al., 2021).

After obtaining the ISA candidate samples, we randomly selected 2~~,~~500 ISA$_{RS}$ and ISA$_{OSM}$ samples,~~,~~ respectively, within each hexagon as the final ISA training samples (see Section 5.3 for details). It can be seen that the~~our~~ generated ISA samples cover a~~ed~~ broad terrestrial surface, especially in India and China, where a large number of small villages are found~~gather~~ (Fig. 4).

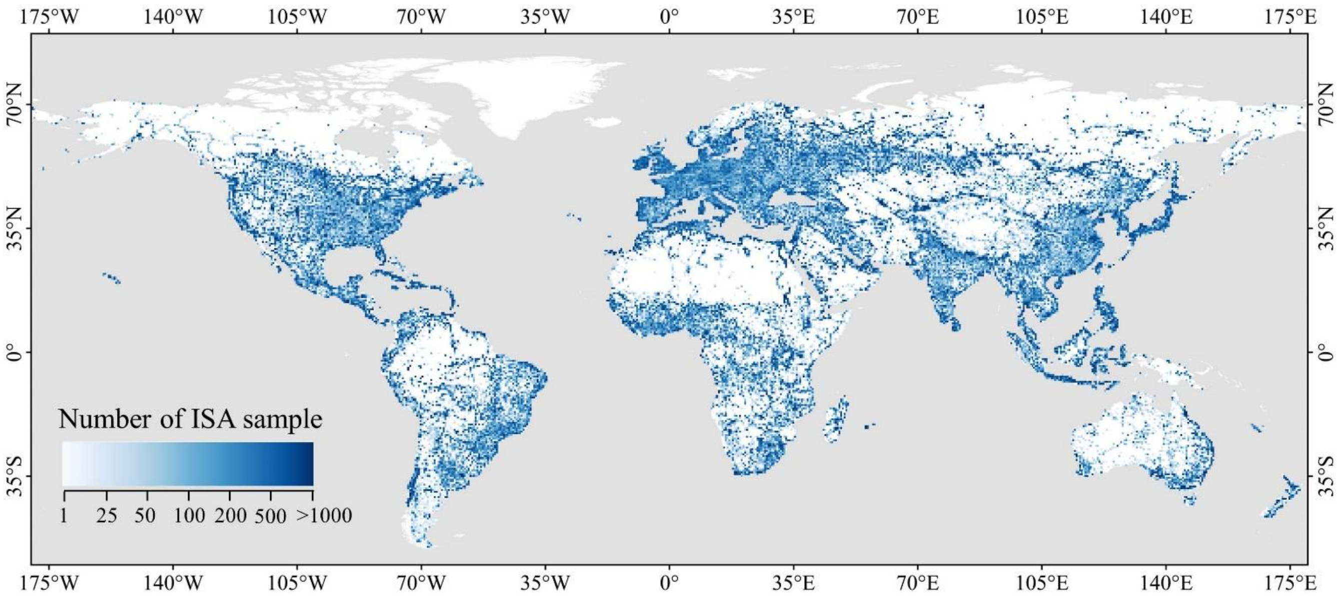

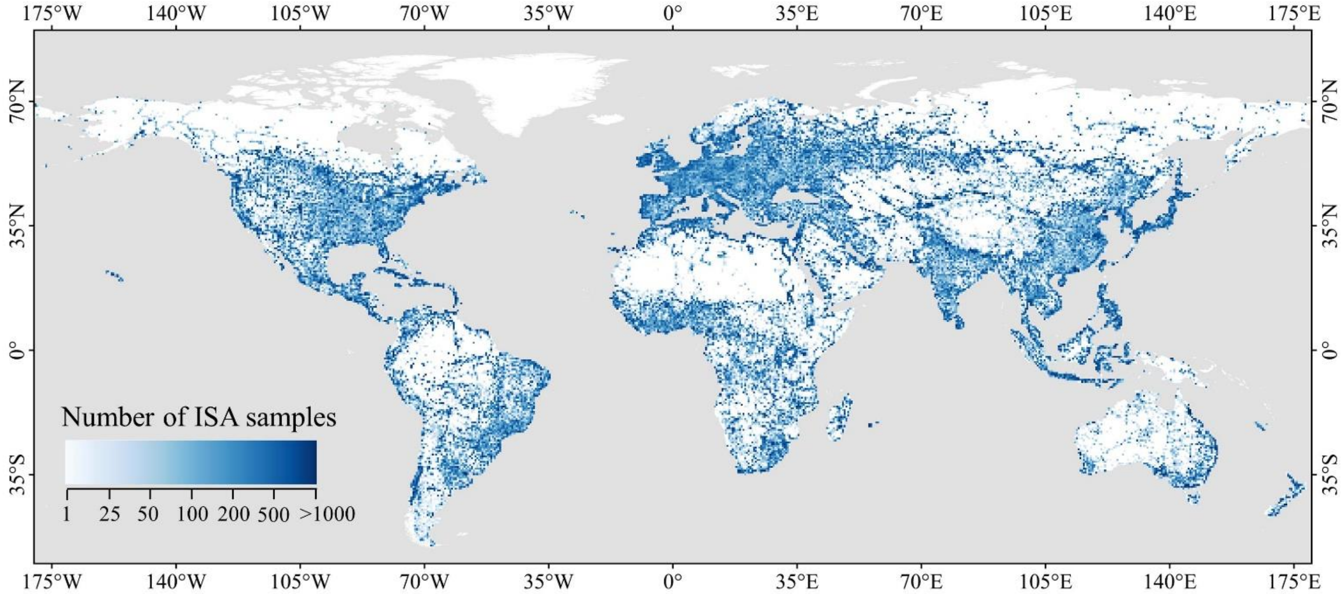

Figure 4. Global distribution of ISA training samples. The number of samples was counted within 0.5~~°~~° spatial grid.

On the other hand, NISA (non-ISA) training samples a~~we~~re also important for accurate ISA mapping. We used the three existing datasets (i.e., GISA 30 m~~m~~, FROM_GLC10, GlobeLand30) and the OSM to generate the NISA samples. Firstly, we took the intersection of the NISA regions in the three datasets as the initial NISA sample pool:

$$NISA = NISA_{GISA} \cap NISA_{GlobeLand30} \cap NISA_{FROM\_GLC10} - ISA_{OSM} \quad (1)$$

For GlobeLand30 and FROM_GLC10, NISA i~~wa~~s defined as all the land~~-~~cover types other than ISA. We ~~then~~ masked the initial NISA sample pool using the OSM buildings and roads to suppress the errors in the existing global datasets. To this end, ~~here~~ we used the OSM version built in December 2020[2], which documents~~ed~~ more buildings and road networks than the 2017 version. ~~Besides~~In addition, ~~,~~ we buffered the OSM roads with a 30~~-~~m buffer to ~~better~~ mitigate the errors. Subsequently, 30,000 points were randomly selected in each hexagon as NISA samples. The distance between each NISA sample was kept larger than 200 ~~-~~m, to ensure the~~its~~ diversity and irrelevance. Finally, we extracted 58 million training samples (51,674,533 NISA samples and 6,897,378 ISA samples) for the GISA-10m mapping.

Table 2. The multi-source features used for the GISA-10m mapping.

Type	Features	Description	Dimension	Source

[2] https://planet.openstreetmap.org/planet/2020/planet-201207.osm.bz2, last accessed: 13 Mar 2021

Spectrum	Blue, green, red, red edge_1, red edge_2, red edge_3, NIR, red edge_4, SWIR_1, and SWIR_2	50th percentile value of the reflectance derived from all the available Sentinel-2 images	10	Sentinel-2
Normalized indices	Index1, Index2, Index3, Index4, Index5, Index6, Index7, Index8, Index9, Index10, Index11, Index12, Index13, Index14, Index15	Normalized indices derived from the spectral bands describ~~pted~~ed above. The indices we~~a~~re calculated as: Index1=NI (NIR, blue), Index2=NI (NIR, green), Index3=NI (NIR, red), Index4=NI (NIR, red edge_1), Index5=NI (NIR, red edge_2), Index6=NI (NIR, red edge_3), Index7=NI (NIR, red edge_4), Index8=NI (SWIR_1, blue), Index9=NI (SWIR_1, green), Index10=NI (SWIR_1, red), Index11=NI (SWIR_1, NIR), Index12=NI (SWIR_2, blue), Index13=NI (SWIR_2, green), Index14=NI (SWIR_2, red), Index15=NI (SWIR_2, NIR), where NI represents the function (b1−~~–~~b2) / (b1+ b2), and b1 and b2 denote two spectral bands	15	Sentinel-2
SAR	VV, VH	Temporal mean VV and VH backscatter coefficients of the Sentinel-1 images	2	Sentinel-1
Temporal statistics	NDVI_Std, MNDWI_Std, NDBI_Std, NDVIMax, VV_Std, VH_Std	Standard deviation of NDVI, MNDWI, NDBI, VV and VH backscatter coefficients; m~~M~~aximum ND~~I~~VI of the year	5	Sentinel-1 & Sentinel-2
Texture	Contrast, dissimilarity, entropy, IDM, ASM	The GLCM texture derived from the NIR band of the Sentinel-2 data, including entropy, dissimilarity, contrast, angular second moment (ASM), and inverse difference moment (IDM)	5	Sentinel-2
Topography	Elevation, slope, and aspect	Slope and aspect calculated from the elevation	3	SRTM & GMTED

3.1.2 Multi-source feature extraction

The dedicated image pyramid of the GEE platform enabled us to perform pixel-wise feature extraction (Gorelick et al., 2017). Therefore, based on all the available Sentinel data for~~in~~ 2016, we constructed a set of spectral, phenological, textural~~e~~, SAR, and topographical features with the temporal composite method (Table 2). This approach used all the available data, and at the same time allowed us to reduce the feature dimension, preserve the temporal information, and minimize the effects of~~from~~ clouds and shadows (Yang and Huang, 2021). Firstly, we used the spectral signatures provided by the ~~Sentienl~~Sentinel-2 data to extract the ISA in the visible, red-edge, ~~near-infrared~~NIR, and infrared bands (Table 2). Moreover, considering that spectral indices can~~ould~~ increase the differences between land covers, we also extracted a series of normalized spectral indices to enhance the discriminative~~on~~ ability between ISA and NISA (Yang and Huang, 2021) (Table 2). These indices were built according to the following criteria: ~~(~~1) t~~T~~hey were mainly constructed by ~~near-infrared~~ the ~~(~~NIR~~)~~ and ~~short-wave infrared (~~SWIR~~)~~ bands, due to their better atmospheric transmission (Huang et al., 2021; Yang and Huang, 2021); and ~~(~~2) e~~E~~ach index contained at least one 10-m band (i.e., visible and NIR bands), to ensure the spatial resolution of the features.

The complex spectral and spatial characteristics in urban environments increase the difficulty of ISA mapping. In this regard, textural~~e~~ features are usually employed to depict the spatial information of urban ISA (Huang and Zhang, 2013). To further exploit the textural information for the ISA mapping, we computed the gray-level co-occurrence matrix (GLCM) via the NIR band, to depict the spatial information of urban ISA. Owing to the high redundancy among GLCM measurements (Clausi, 2002), we chose the contrast, dissimilarity, entropy, ~~IDM (~~inverse difference moment (IDM), and ~~ASM (~~angular second moment (ASM) for the texture extraction (Rodriguez-Galiano et al., 2012). The window size for the GLCM measurements was set to 7 × 7 as this~~it~~ i~~wa~~s suitable for urban classification with an image resolution from 2.5 to 10 -m (Puissant et al., 2005). ~~Besides~~In addition, we averaged the GLCM from different directions (0, 45, 90, and 135°) to maintain the rotational invariance (Rodriguez-Galiano et al., 2012).

Given that the spectra and backscatter of some NISA (e.g., vegetation and water bodies) vary throughout time, the phenological information derived from the multi-temporal spectral and SAR data wa~~i~~s utilized to depict the temporal fluctuations. We calculated the maximum NDVI as well as the standard deviation of the NDVI (Tucker, 1979), MNDWI (Xu, 2006), and ~~NDBI (~~normalized difference built-up index (NDBI) (Zha et al., 2003), to further enhance the temporal information. These temporal characteristics a~~we~~re useful in identifying NISA with temporal fluctuations. For example, the spectra of fallow cropland and ISA a~~we~~re similar, and even SAR data may not ~~well~~ separate them well. However, the NDVI of cropland can describe the changes of crop~~s~~ growth, and hence~~,~~ its standard deviation can be used to distinguish between ISA and cropland. In addition, to increase the robustness of these temporal features, Sentinel-2 data from ~~adjacent~~ two adjacent years were also ~~included~~considered.

SAR data have the~~is~~ potential to~~for~~ reduc~~eing~~ the false alarms caused by bare soil in optical images, and are~~it is~~ more sensitive to buildings. In addition, ~~it is able~~SAR signals can~~to~~ penetrate clouds. Therefore~~So~~, in this study, SAR data were~~it was~~ combined with optical data for the ISA mapping. Specifically, the ~~VV (~~vertical-vertical (VV) polarization~~)~~ and ~~VH~~ the ~~(~~vertical-horizontal (VH) polarization~~)~~ backscatter coefficients from the ~~Sentienl~~Sentinel-1 images were selected. ~~Specifically,~~ B~~b~~ased on all the available ~~Sentienl~~Sentinel-1 data, the annual mean and standard deviation of the VV and VH backscatter coefficients were calculated by the temporal composite method:

$$\sigma_{mean} = \frac{1}{n}\sum_{i=1}^{n}\sigma_i \tag{2}$$

$$\sigma_{std} = \sqrt{\frac{\sum_{i=1}^{n}(\sigma_i-\sigma_{mean})^2}{n}} \tag{3}$$

where n denotes the total number of Sentinel-1 observations within a year, and σ_i represents the ith backscatter coefficient observation in the year. The temporal composite~~mean~~ method can reduce the speckle noise in ~~the~~ SAR image~~rys~~ (Lin et al., 2020), while the annual standard deviation can reflect the temporal information. Topography-related features are also necessary for ISA mapping, in order to reduce the confusion between complex terrain and buildings. For instance, topographical features can~~ould~~ help to distinguish steep~~ly~~ hills from buildings (Gamba and Lisini, 2013). Specifically, we used ~~SRTM (~~Shuttle Radar Topographic Mission (SRTM) digital elevation model (DEM) data in the areas below 58° latitude and ~~GMTD2010 (~~Global Multi-resolution Terrain Elevation Data 2010 (GMTED2010) in the areas above 58° (Huang et al., 2021). Finally, a total of 41 features were constructed from~~on~~ the 2.7 million Sentinel images (2,613,180 Sentinel-2 and 122,156 Sentinel-1) and DEM data.

3.1.3 Hexagon-based adaptive random forest classification

When dealing with global land~~-~~cover classification, the global terrestrial surface i~~wa~~s usually divided into homogeneous sub-regions according to criteria such as climate, land cover, or administrative regions (Goldblatt et al., 2018). For global ISA mapping, regular square grids a~~we~~re commonly used (Table 1), such as 1° and 5° grids (e.g., WSF2015 and GLCFCS). ~~Herein~~ In this study, we divided the terrestrial surface into 2° hexagonal grid cells~~s~~ (Fig. 1), due to the~~its~~ symmetry and invariance (You et al., 2021). ~~Besides~~Furthermore, there were no gaps or overlaps between hexagons, and the distance between adjacent hexagon centers was approximately equal (Richards et al., 2000).

The ~~Random forest (~~RF~~)~~ classifier has been widely used in global ISA mapping, due to its robustness to erroneous samples, flexibility with~~to~~ high-dimensional data, and tolerance to noise (Bauer and Kohavi, 1999; Wulder et al., 2018) (Table 1). The RF classifier~~It~~ utilizes ensemble learning to obtain predictions by voting on categories through multiple decision trees (Breiman, 2001). Each tree uses a random subset of the input features to increase the generalization ability. In addition, trees are grown from different subsets of training data (i.e., bagging or bootstrapping), to increase the diversity (Rodriguez-Galiano et al., 2012). RF has been ~~proved~~ shown to outperform other classifiers when dealing with large-scale and high-dimensional data (Goldblatt et al., 2016). The ~~flexibility~~ ability of RF to handle multi-source data also makes it convenient ~~for us to~~when dealing with Sentinel radar and optical data. Therefore, together with the afore-mentioned multi-source features and global training samples, the RF classifier was used for the GISA-10m mapping. As suggested by Yang and Huang~~,~~ (2021), the number of trees was set to 200. We divided the global terrestrial surface ~~using~~ into 1,808 hexagons, ~~where~~ and a local RF model was built for adaptive ISA classification in each hexagon. Therefore, a total of 1,808 RF models were built. In terms of the features used to train each tree, the random forest uses a random subset of features to reduce the correlation between trees. In general, the diversity of the trees can be increased when fewer features are used for training each tree (Breiman, 2001). In the GISA-10m mapping, we set the number of features used for each tree to the square root of the total number of features, as suggested by Liu et al.~~,~~ (2020b).

3.2 Accuracy assessment

The test samples for~~of~~ GISA-10m included: ~~(~~1) visually interpreted samples via Google Earth;~~,~~ ~~(~~2) test samples extracted from ~~the~~ ZiYuan-3 (ZY-3) built-up datasets (Liu et al., 2019);~~,~~ and ~~(~~3) building samples located in ~~the~~ arid areas.

(1) As suggested by Stehman and Foody (2019), we used cluster sampling to collect the visually ~~-~~interpreted test samples. The primary sampling unit involved 59 grid cells~~s~~ with a side length of 1°, which were~~as~~ randomly selected based on population, ecoregion, and urban landscape (the red squares in Fig. 5). The secondary sampling unit included the random samples within each grid cell. In such a way, samples from different urban sizes and densities were considered for the validation. Specifically, in each grid cell, we randomly selected 100 ISA and 100 NISA points to test their accuracy. An equal allocation of ISA and NISA test samples could reduce the bias of the accuracy assessment, and hence allow for a more accurate estimation~~e~~ of the user'~~'~~s accuracy (Olofsson et al., 2014; Stehman, 2012). By referring to ~~the~~ high-resolution Google Earth images, a pixel

(10 m~~m~~ × 10 m~~m~~) was labeled~~led~~ as ISA if more than half of its area was covered by ISA;~~,~~ otherwise, it was identified as NISA. As can be seen ~~from~~in Fig. 5, the test samples involved not only high-density ISA samples from~~in~~ urban areas, but also a large number of low-density samples from~~in~~ suburban and rural regions. Finally, a total of 11,800 test samples were obtained.

(2) Liu et al.~~,~~ (2019) proposed a multi-angle built-up index to extract built-up areas from ZY-3 images covering 45 global cities, which obtained~~ith~~ an overall accuracy (OA) of greater than 90%. The multi-angle ZY-3 images depict~~ed~~ the three-dimensional and vertical structure of buildings, which ~~w~~is~~ere~~ more effective and accurate than ~~the~~ planar feature extraction for detecting built-up areas. Given the higher spatial resolution (2 ~~-~~m) and better accuracy of the ZY-3 global built-up dataset, we extracted test samples from it for~~in~~ the year of 2016 (Huang et al., 2021a; Liu et al., 2019). A sample (10 m~~m~~ × 10 m~~m~~) was labeled~~led~~ as ISA if more than 50% of its area was classified as ISA in the ZY-3 dataset, while the NISA samples were those with no built-up pixels in the area (Huang et al., 2021a). For each city, the number of samples was proportional to the area of the ZY-3 image, and the ratio of ISA and NISA test samples was consistent with the ratio of the built-up and non-built-up classes (Huang et al., 2021a). In this way, we obtained 47,216 NISA samples and 21,152 ISA samples (the green dots in Fig. 5) from 24 cities in the ZY-3 built-up dataset.

(3) Considering the difficulty of ISA extraction in ~~the~~ arid regions (Tian et al., 2018), we paid special attention to the accuracy assessment in the arid regions. To this end, we visually interpreted 5,385 building pixels in these regions. A total of 25 photo interpreters were recruited for this task by referring to the Google Earth images. These samples were then further checked by three experts. The arid regions were defined according to the “~~"~~d~~D~~eserts and x~~X~~eric s~~S~~hrublands”~~"~~ biome in Olson et al.~~,~~ (2001).

Based on the three groups of test samples aforementioned, the accuracy of GISA-10m was assessed using the~~by~~ ~~overall accuracy (~~OA~~)~~, kappa, producer’~~'~~s accuracy (PA), user’~~'~~s accuracy (UA), and F1-s~~S~~core (the harmonic mean of the PA and UA). ~~Besides,~~ S~~s~~even existing global ISA datasets were used for the inter-comparison with GISA-10m, ~~including~~ i.e., GHSL 2018, GLCFCS, WSF2015, FROM_GLC10, GISA, GAUD, and GAIA (Table 1). The three groups of test samples mentioned above were used to assess and compare the accuracy of these products.

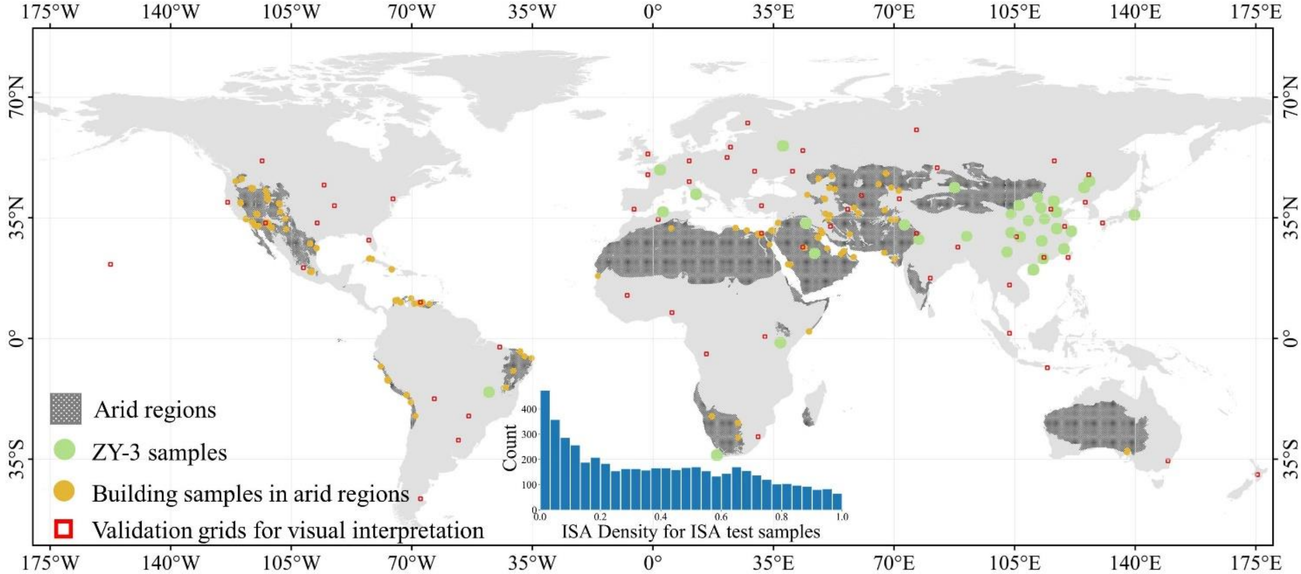

Figure 5. Global distribution of the test samples and grid used in this study, including (1) 59 grids for visual interpretation, (2) ZY-3 reference set covering 23 cities, and (3) 5,385 building samples in the arid regions. The arid regions were extracted from “~~"~~d~~D~~eserts and x~~X~~eric s~~S~~hrublands”~~"~~ biome in Olson et al.~~,~~ (2001). The inner graph shows the~~ed~~ ISA density within the 0.5-~~-~~km buffer for the~~of~~ ISA test samples.

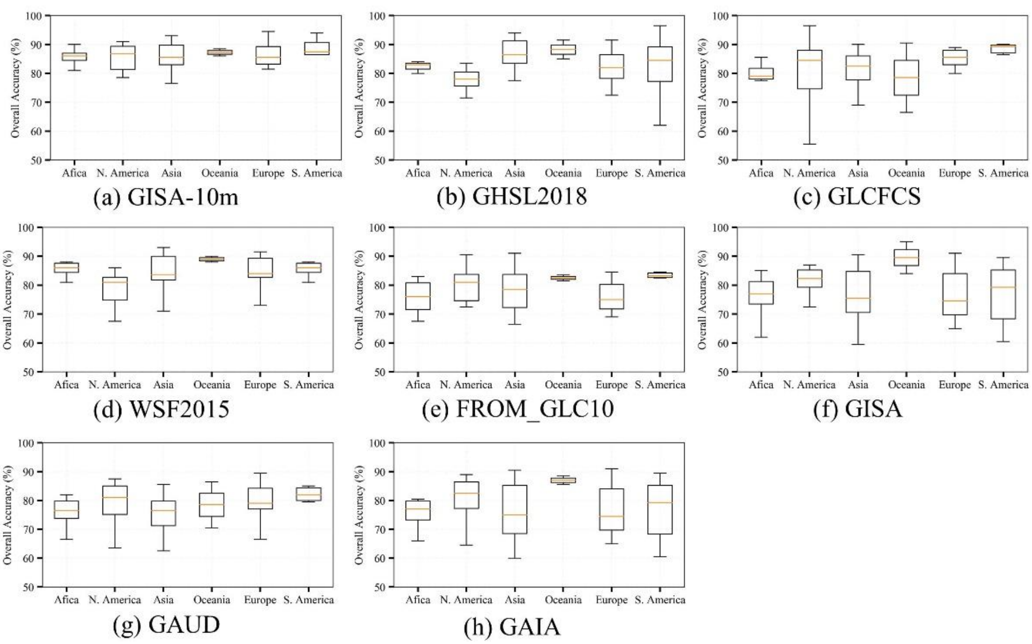

Figure 6. Box plots of the overall accuracy for GISA-10m and existing datasets in the six continents.

4 Results

4.1 Accuracy assessment of GISA-10m

4.1.1 Global scale

The accuracy assessment based on the visually ~~-~~interpreted samples is~~were~~ shown in ~~the~~ Table 3. GISA-10m exhibits~~ed~~ the highest OA of 86.06%, ~~with~~ representing an increase in OA of +2.73%, +3.73%, and +2.3%~~, respectively,~~ over~~with respect to~~ GHSL 2018, GLCFCS, and WSF2015, respectively (Table 3). The k~~-K~~appa of GISA-10m i~~wa~~s 0.7165, which exceeds~~ed~~ ~~the~~ WSF2015, FROM_GLC10, and GAIA by 0.052, 0.1774, and 0.2039, respectively. ~~Alongside,~~ GISA-10m also shows~~ed~~ a higher accuracy than~~as to~~ the 30~~-~~m resolution datasets (i.e., GISA, GAUD, GAIA), which suggests~~ed~~ a better delineation of global ISA, due to the~~its~~ higher resolution. Fig. 6 summarizes~~d~~ the results of the accuracy assessment at the continent level, with the average and standard deviation of the OA for each continent shown in the box plots. ~~In general~~Overall, GISA-10m exhibits a~~ed~~ stable performance for each continent, with an average OA of more than 85%. Specifically, Oceania and South America ~~obtained~~ show the best OAs of 87.25% and 87.08%, followed by Europe (86.45%) and Asia (85.85%). The results also show~~ed~~ that the average OA~~overall accuracy~~ of GISA-10m exceeds that of~~ed~~ the existing datasets in Africa, North America, and Europe. In addition, it ~~was found~~is apparent that the performance of GHSL 2018 and GLCFCS ~~wa~~is~~s~~ relatively unstable in South America and North America, respectively.

Table 3. Results of quantitative accuracy assessment via visually-interpreted and ZY-3 samples between GISA-10m and the existing ISA datasets. OA represents the overall accuracy.

Global~~e~~	Visually interpreted samples (n = 10800)				ZY-3 samples (n = 68368)			
	OA (%)	Kappa	F1-score of ISA (%)	F1-score of NISA (%)	OA (%)	Kappa	F1-score of ISA (%)	F1-score of NISA (%)
GISA-10m	**86.06**	**0.7165**	**83.65**	**88.55**	**86.25**	**0.6664**	76.25	**90.32**
GHSL 2018	83.33	0.6540	78.66	86.89	84.53	0.6401	75.27	88.74
GLCFCS	82.33	0.6336	77.57	85.96	84.56	0.6280	73.68	89.08
WSF2015	83.76	0.6645	79.68	87.06	85.44	0.6664	**77.35**	89.27
FROM_GLC10	78.16	0.5391	69.65	83.39	83.66	0.6082	72.39	88.39
GISA	78.84	0.5532	70.65	83.88	85.63	0.6627	76.65	89.63
GAUD	77.36	0.5185	67.46	83.01	85.59	0.6549	75.70	89.76
GAIA	77.05	0.5126	67.13	82.77	84.23	0.6381	75.39	88.40

GISA-10m obtains~~ed~~ the best OA of 86.25% on the ZY-3 samples, outperforming ~~GHSL2018~~GHSL 2018, GLCFCS, and WSF2015~~,~~ by 1.72%, 1.69%, and 0.81%, respectively. The ZY-3 images employed by Liu et al.~~,~~ (2019) covered 45 major global cities, and therefore the ZY-3 samples were more inclined to reflect the accuracy in urban regions. Therefore, the accuracy difference between the various datasets i~~wa~~s not significant (Table 3). Due to the relatively coarse~~r~~ resolution, the

30-~~–~~m datasets usually tend~~ed~~ to overestimate the ISA extent (Gong et al., 2020b), resulting in a higher UA but lower PA (Table S1). For example, the ISA UA of GISA i~~wa~~s slightly higher than that of GISA-10m, but its PA i~~wa~~s much smaller ~~than the latter~~ (Table S1). However, when the two metrics (PA and UA) a~~we~~re considered at the same time (i.e., the F1-s~~S~~core), GISA-10m outperforms~~ed~~ GISA.

4.1.2 Rural, arid, and urban regions

The population of rural regions is comparable to that of urban regions (https://data.worldbank.org/). The e~~E~~xisting studies, as well as their global ISA datasets, have usually focused on the performance in urban regions, and~~but~~ the accuracy of the rural ISA regions has not been sufficiently assessed. Hence, in this study, we paid special attention to the accuracy assessment in the global rural regions. Specifically, we divided the GISA-10m into urban and rural regions using the urban boundary defined by Li et al.~~,~~ (2020). In fact, due to the random sampling strategy, most of the visually ~~-~~interpreted test samples were located in rural regions.

In the case of the visually ~~-~~interpreted samples, GISA-10m exhibits~~ed~~ a better OA of 86.19% than~~against the GHSL2018~~GHSL 2018 (84.92%), GLCFCS (83.25%), FROM_GLC10 (78.83%), and WSF2015 (83.81%). As regards the three 30-m datasets (i.e., GISA, GAIA, GAUD), their ISA accuracy (F1-score) decreases~~d~~ significantly in the rural regions, while the NISA accuracy i~~wa~~s relatively stable (Tables 2–~~&~~3). Taking~~Having~~ a closer look at the PA, it is apparent~~one can notice~~ that the ISA PA decreases by more than 15% for all ~~the~~ three 30-m datasets (Table S2), which suggests that~~ed~~ there are~~ir~~ more omission errors in the rural regions (Fig. 12b). This demonstrates~~ed~~ the deficiency of the 30-m datasets in depicting rural ISA, and also reflects~~ed~~ the importance of 10-m global ISA mapping.

Table 4. Results of quantitative accuracy assessment via visually-interpreted and ZY-3 samples in rural regions between GISA-10m and the existing ISA datasets. OA represents the overall accuracy.

Rural regions	Visually interpreted samples (n = 9547)				ZY-3 samples (n = 43950)			
	OA (%)	Kappa	F1-score of ISA (%)	F1-score of NISA (%)	OA (%)	Kappa	F1-score of ISA (%)	F1-score of NISA (%)
GISA-10m	**86.19**	**0.6794**	**77.96**	**90.48**	**90.85**	**0.4768**	52.46	**94.94**
GHSL 2018	84.92	0.6297	73.34	89.88	88.95	0.4656	**52.82**	93.74
GLCFCS	83.25	0.5871	70.15	88.72	89.46	0.4261	48.33	94.13
WSF2015	83.81	0.6012	71.17	89.12	89.37	0.4514	51.05	94.04
FROM_GLC10	78.83	0.4485	57.08	86.24	88.59	0.3884	45.08	93.63
GISA	77.87	0.4082	52.53	85.80	89.83	0.3954	44.66	94.40
GAUD	76.38	0.3516	46.13	85.05	89.70	0.3199	36.35	94.40
GAIA	75.41	0.3213	43.05	84.49	88.93	0.3611	41.85	93.88

Table 5. Results of quantitative accuracy assessment via visually-interpreted and ZY-3 samples in arid regions between GISA-10m and the existing ISA datasets. OA represents the overall accuracy.

Arid Region	Visually interpreted samples (n=1020)				ZY-3 samples (n=10827)			
	OA (%)	Kappa	F1-score of ISA (%)	F1-score of NISA (%)	OA (%)	Kappa	F1-score of ISA (%)	F1-score of NISA (%)
GISA-10m	**86.67**	**0.7358**	86.05	**88.22**	**89.64**	**0.7296**	**79.95**	**93.01**
GHSL 2018	86.57	0.7336	**86.06**	87.99	85.13	0.5817	67.68	90.34
GLCFCS	82.16	0.6454	80.32	84.46	85.14	0.6232	72.45	89.82
WSF2015	82.45	0.6516	80.95	84.56	88.37	0.6881	76.53	92.27
FROM_GLC10	76.27	0.5271	70.97	80.59	84.06	0.5755	68.18	89.37
GISA	80.20	0.6058	76.89	83.39	87.72	0.6795	76.23	91.72
GAUD	77.06	0.5424	71.88	81.20	88.66	0.6894	76.37	92.54
GAIA	77.45	0.5506	72.84	81.35	85.78	0.6317	72.79	90.37

Furthermore, we also focused on the accuracy assessment in arid regions. In general, the OA of GISA-10m i~~wa~~s higher than that of the existing datasets (Table 5). Although its ISA UA does~~id~~ not always outperform the other datasets, GISA-10m achieves~~d~~ the highest PA ~~among the existing ones~~ (Table ~~S3~~S4). Specifically, GISA-10m exhibits~~ed~~ a notably higher ISA PA ~~compared to~~than GLCFCS, FROM_GLC10, GISA, GAUD, and GAIA (Table S3), indicating its ~~better~~ superior ability to~~of~~ detect~~ing~~ ISA in arid regions (Fig. 7). Moreover, the accuracy of these global ISA products was assessed using the~~our~~ manually and randomly chosen rural building samples (see Section 3.2). It can be found that GISA-10m detects~~ed~~ 15% more buildings in arid regions ~~with respect to~~than FROM-GLC10, GAUD, and GAIA (Table ~~S4~~S5), which ~~again~~ further verifies~~d~~ its ~~better~~superior performance in describing rural ISA.

In the case of urban regions, GISA-10m exhibits a~~ed~~ satisfactory result, with an OA~~overall accuracy~~ similar to that of the global assessment (Table ~~6~~S4). Note that urban ISA only accounts for one-third of global ISA, while nearly 70% of ISA i~~wa~~s located in suburban and rural regions. The e~~E~~xisting datasets show~~ed~~ relatively more ISA omissions in rural and~~or~~ arid regions, suggesting that global ISA mapping at a 10-m resolution (e.g., GISA-10m) is necessary. Moreover, we divided the visually ~~-~~interpreted samples located in cities into three levels (i.e., small, medium~~iddle,~~ and large~~big~~ cities) to assess the accuracy of GISA-10m ~~over~~ for cities of~~with~~ different scales, i.e., ~~:~~ Level 1 (population < 250,000), Level 2 (250,000 to 1,000,000), and Level 3 (>1,000,000) (Yang et al., 2019). ~~It was found that~~ T~~t~~he OA~~overall accuracy~~ of GISA-10m across the three levels of cities i~~wa~~s 85.35%, 87.43%, and 85.42%, respectively (Table ~~S5~~S6). These results indicate~~d~~ that the performance of GISA-10m in different scales of cities i~~wa~~s stable, and ~~was~~ the results are also close to the~~its~~ global assessment result (OA of 86.06%).

~~**Table 6. Results of quantitative accuracy assessment via visually-interpreted and ZY-3 samples in urban regions between GISA-10m and the existing ISA datasets. OA represents the overall accuracy.**~~

Urban Regions	Visually interpreted samples (n=2253)				ZY-3 samples (n=24418)			
	OA (%)	Kappa	F1-score of ISA (%)	F1-score of NISA (%)	OA (%)	Kappa	F1-score of ISA (%)	F1-score of NISA (%)
GISA-10m	**85.49**	**0.30**	**91.93**	**38.26**	77.96	**0.52**	82.71	**69.61**
GHSL 2018	76.61	0.20	86.02	31.41	76.56	0.47	82.38	64.99
GLCFCS	78.43	0.18	87.51	27.96	75.75	0.48	80.98	66.55
WSF2015	83.58	0.23	90.73	32.76	**78.36**	0.49	**84.64**	63.38
FROM_GLC10	75.32	0.21	85.15	31.66	74.78	0.45	80.35	64.80
GISA	82.96	0.24	90.41	33.15	78.09	0.49	84.25	63.98
GAUD	81.49	0.22	89.49	31.06	78.20	0.50	84.07	65.48
GAIA	84.02	0.20	91.07	29.57	75.77	0.41	83.30	55.83

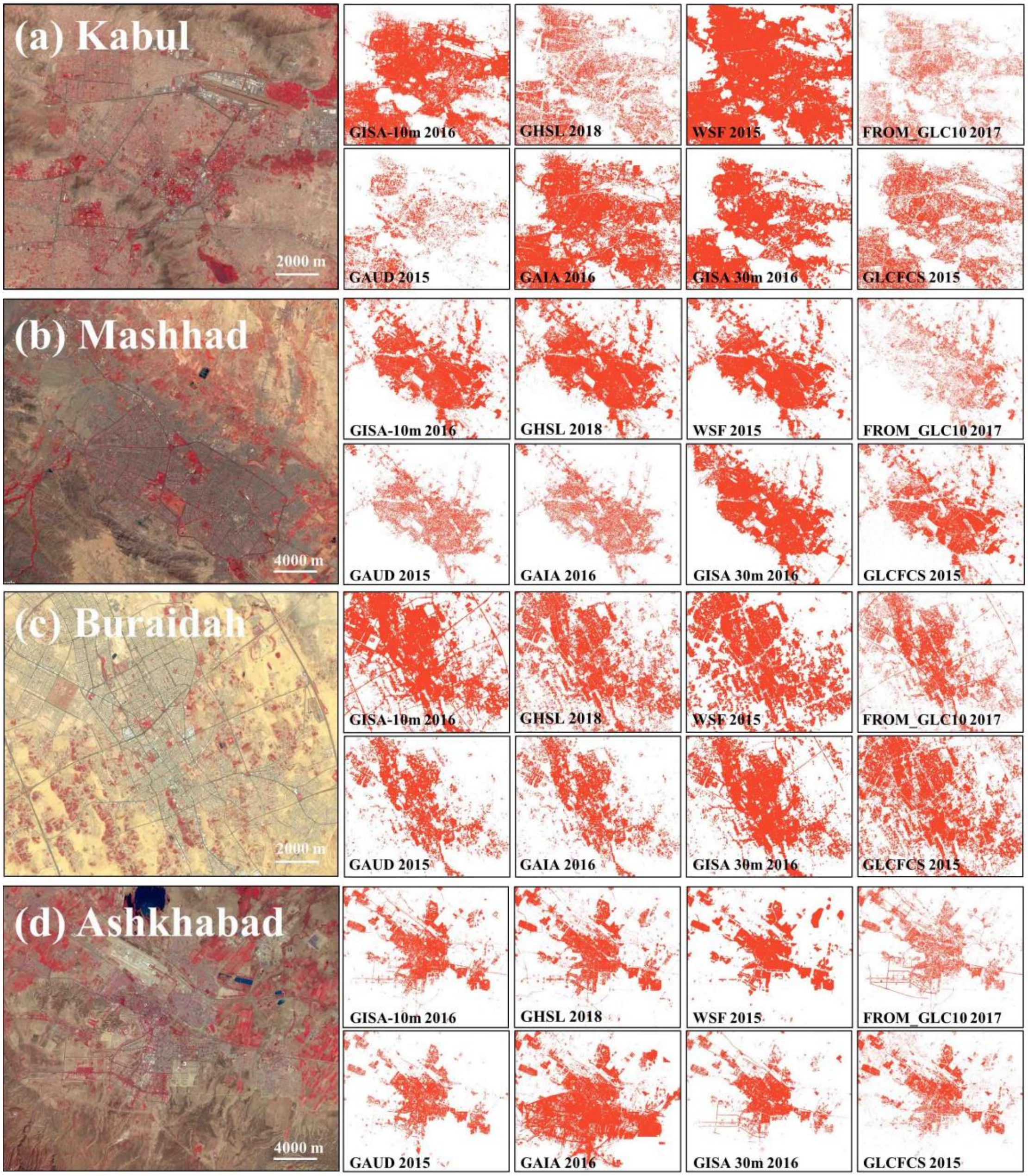

Figure 7. Comparison of the GISA-10m and the other datasets over arid regions in: (a) Kabul, Afghanistan; (b) Mashhad, Iran; (c) Buraidah, Saudi Arabia; (d) Ashkhabad, Turkmenistan. The illustration is of Sentinel-2 images with a false-color combination (R: NIR, G: r~~R~~ed, B: g~~G~~reen) to enhance the ISA.

4.2 Global ISA distribution

4.2.1 Urban and rural ISA

Based on the GISA-10m, we analyzed the global ISA distribution at a 10-m scale (Fig. S1). Global ~~impervious surface area~~ISA i~~wa~~s mainly distributed in Asia (41.43%), North America (20.59%), and Europe (18.93%), followed by Africa (9.78%) and South America (7.50%). It i~~wa~~s found that 67% of global ISA i~~wa~~s located in the Eastern Hemisphere, while 85% of ISA i~~wa~~s distributed to~~in~~ the north of the equator. Rural ISA i~~wa~~s more scattered than urban ISA (Fig. S1), and is~~t was~~ mainly located in Asia (42.84%), Europe (19.49%), and North America (16.51%). Asia ~~embraced~~ has the largest urban ISA, which is more than twice that of~~as~~ Europe. Although North America only accounts~~ed~~ for 20% of global ISA, its urban ISA takes~~ook~~ up more than 29% of the global total. Taking a closer look at the ratio of rural and urban ISA (Table ~~7~~6), ~~one can see~~it can be seen that rural ISA is~~were~~ 2.2 times larger than~~ the~~ urban ISA. At the continental level, Africa possesses~~d~~ the highest “~~"~~rural-to-urban ratio”~~"~~, which ~~may be~~is likely related to its large population but relatively poor economy.

Table ~~7~~6. Impervious surface area derived from GISA-10m in the six continents.

ISA	Europe	Africa	S. America	Oceania	N. America	Asia	Global~~e~~
Total (10^5 km^2)	1.88 (18.93%)	0.97 (9.78%)	0.75 (7.50%)	0.18 (1.76%)	2.05 (20.59%)	4.12 (41.43%)	9.94 (100%)
Rural (10^5 km^2)	1.33 (19.49%)	0.78 (11.43%)	0.55 (8.11%)	0.11 (1.62%)	1.13 (16.51%)	2.93 (42.84%)	6.84 (100%)
Urban (10^5 km^2)	0.55 (17.69%)	0.19 (6.16%)	0.19 (6.17%)	0.07 (2.07%)	0.92 (29.56%)	1.19 (38.35%)	3.10 (100%)
Rural/u~~U~~rban	2.42	4.08	2.89	1.73	1.22	2.46	2.20

At the country scale, China and the ~~United States (~~US~~)~~ ~~embraced~~account for 33% of global ISA. Together with Russia, Brazil, India, Japan, Indonesia, France, Canada and Germany, these ten countries account~~ed~~ for 58% of the world ISA. The urban ISA ~~owned by~~of the top ten countries (US, China, Russia, Brazil, Japan, India, Mexico, France, Germany, and the United Kingdom) ~~took~~ makes up 69% of the global total, while the top ten countries in terms of rural ISA (China, US, Russia, Brazil, India, Indonesia, Japan, France, Canada, and Germany) account~~ed~~ for only 54% of the total. In Africa, the Republic of South Africa has~~d~~ much more urban ISA than the other countries. However, Nigeria has a~~showed~~ comparable rural ISA to ~~the~~ South Africa (~7738 km^2). China ranks~~ed~~ first in terms of rural ISA, most of which i~~wa~~s located in the North China Plain (Fig. ~~9B~~s3b). Indonesia also possesses~~d~~ a lot of~~ much~~ rural ISA, since it ranks~~ed~~ sixth for~~in the~~ rural ISA but ~~its urban ISA~~ only ~~ranked~~ sixteenth for urban ISA.

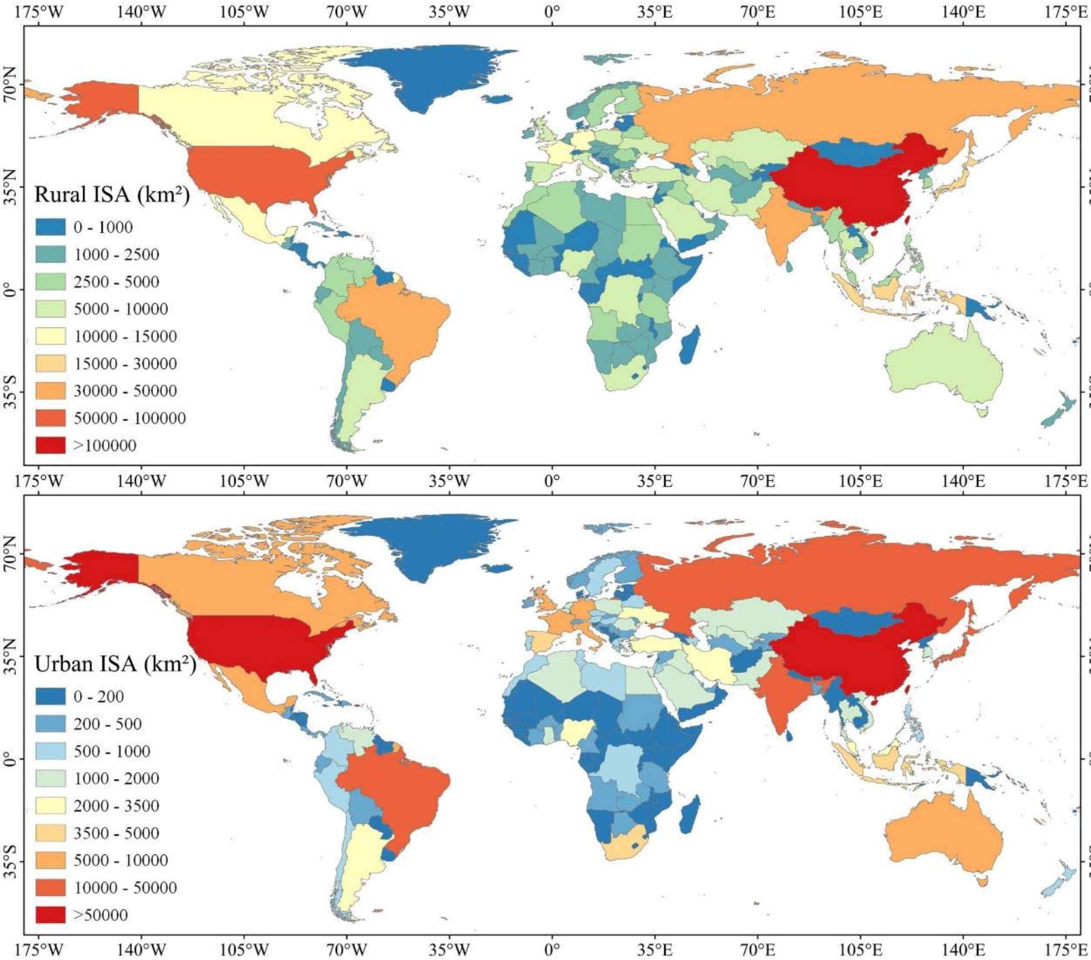

~~Figure 9. Urban and rural ISA at the country scale based on GISA-10m.~~

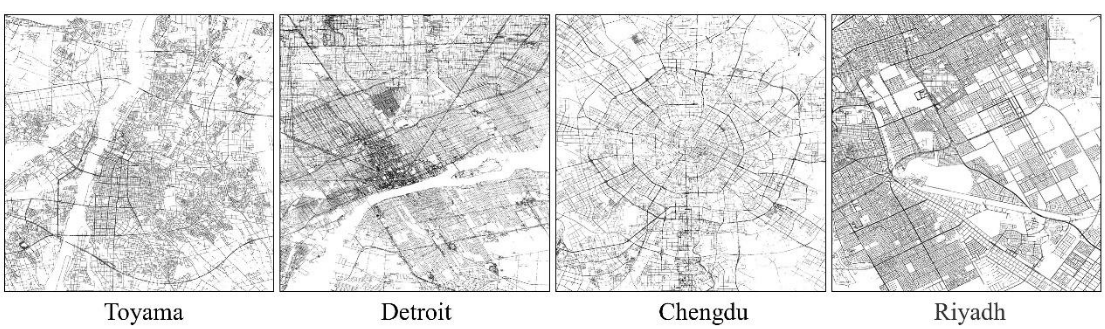

Figure ~~10~~9. Examples of road area derived from GISA-10m and OSM in ~~the~~ Toyama (Japan), Detroit (US), Chengdu (China), and Riyadh (Saudi Arabia).

4.2.2 Global road area

Roads are major anthropic footprints, so we attempted to ~~analyse~~analyze the global road area based on GISA-10m, ~~by~~ courtesy of its high spatial resolution. Firstly, the road networks were extracted from the OSM database, and then~~,~~ the ISA regions in the GISA 10-m data within a 10-m buffer of the road networks were identified as ~~the~~ road areas (Fig. ~~10~~9). The r~~R~~esults show~~ed~~ that 82.84% of the global road area is~~s~~ located in Asia (30.74%), North America (27.17%), and Europe (24.92%), while the remaining 17.16% ~~was owned by~~is found in South America (8.26%), Africa (7.47%), and Oceania (1.44%). Although Asia far exceeds~~ed~~ the other continents with regard to~~ing~~ ISA and rural road area, it possesses~~d~~ ~~less~~a smaller urban road area than North America. China and the US have~~d~~ the largest road area, together accounting for 29% of the global total, ~~which were~~ followed by Brazil, Japan, Russia, Germany, India, France, Indonesia, and Mexico. The top ten countries have ~~owned~~ more than half of the global road areas~~s~~. The global road area accounts~~ed~~ for 14.18% of the global ISA, and the rural road area i~~wa~~s 1.5 times larger than the urban road area (Table ~~8~~7). However, it should be noted that these estimates might be biased owing to the incompleteness of the OSM data. In addition, narrow roads might be partly detected or missed, due to the limitation of the spatial resolution.

Table ~~8~~7. Statistics for the road area derived from GISA-10m and OSM in the six continents.

Road	Europe	Africa	S. America	Oceania	N. America	Asia	Global
Total (10^4 km^2)	3.51 (24.92%)	1.05 (7.47%)	1.16 (8.26%)	0.20 (1.44%)	3.83 (27.17%)	4.34 (30.74%)	14.10 (100%)
Rural (10^4 km^2)	2.27 (26.88%)	0.71 (8.43%)	0.75 (8.88%)	0.11 (1.26%)	1.84 (21.73%)	2.77 (32.82%)	8.45 (100%)
Urban (10^4 km^2)	1.24 (21.99%)	0.34 (6.03%)	0.42 (7.34%)	0.10 (1.70%)	2.00 (35.29%)	1.56 (27.65%)	5.66 (100%)
Rural/Urban	1.82	2.09	1.81	1.10	0.92	1.77	1.49

5 Discussions

5.1 Inter-comparison with the existing datasets

To further validate the performance of GISA-10m, we compared it with ~~a series of~~the existing state-of-the-art global datasets, ~~including~~ i.e., three 10-m resolution datasets (~~i.e.~~ WSF2015, ~~GHSL2018~~GHSL 2018, FROM_GLC10) and four 30-m resolution datasets (~~i.e.~~ GLCFCS, GAUD, GAIA, ~~and~~ GISA). Their spatial agreement~~s~~ with GISA-10m was~~ere~~ measured by the linear fit of the ISA fraction, including metrics such as the correlation coefficient and root-mean-square error (RMSE). Attention was also paid to the~~ir~~ performance of the different products~~s~~ in urban and rural regions, for a comprehensive assessment. Considering the~~ir~~ different~~ce of~~ spatial resolutions, the ISA fraction was calculated within the 0.05° spatial grid.

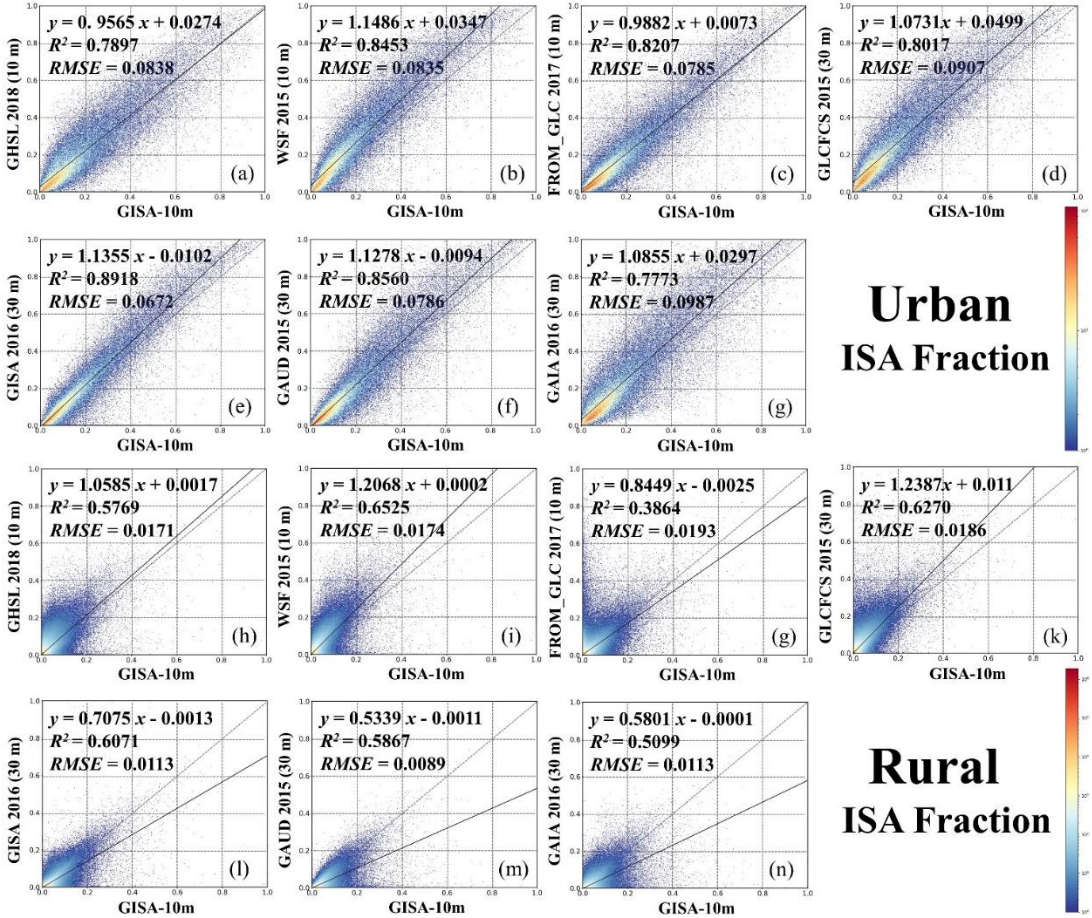

Figure ~~11~~10. Scatterplots of the urban and rural ISA fraction between GISA-10m with GHSL, WSF, FROM_GLC10, GLCFCS, GAUD, GAIA, and GISA, respectively. The ISA fraction was calculated within a 0.05° ×~~by~~ 0.05° spatial grid.

In general, GISA-10m exhibits a~~ed~~ high agreement (0.777 < R^2 < 0.892) with these existing datasets over urban regions. In the case of GHSL_2018 and FROM_GLC10, their fitted lines with GISA-10m a~~we~~re closer to the 1:1 line in the high fraction regions (Figs. ~~11a~~ 10a and ~~&~~c). As shown in ~~the~~ Fig. ~~12~~11, GHSL_2018 and GISA-10m a~~we~~re generally similar in the dense urban areas (e.g., the urban cores in Fig. ~~12~~11), but GHSL_2018 tends~~ed~~ to overestimate ISA in the low-density residential areas (Fig. ~~12c~~11c). The fitted lines for GLCFCS and WSF2015 a~~we~~re above the diagonal (slope greater than 1 and intercept greater than 0) in both the high and low ISA fraction regions, possibly ~~owing~~ due to their overestimation~~s~~. For instance, in the case of Cairo (Fig. ~~12b~~11b), WSF2015 shows~~ed~~ significant overestimation,~~s~~ but the other datasets better depict~~ed~~ the residential areas. According to Marconcini et al.~~,~~ (2020), the overestimation~~s~~ of ~~the~~ WSF2015 may be related to the employment of the coefficient of variation (COV), which reduces~~d~~ the omissions in the rural regions, but at the same time leads to overestimation~~s~~ of the ISA extent. The fitted lines for the three 30-m resolution datasets (i.e., GISA, GAIA, GAUD) a~~we~~re all above the diagonal (Fig. ~~11e~~10e–g), suggesting that they detect~~ed~~ more urban ISA than GISA-10 m. However, in the 30-m resolution datasets, vegetation alongside roads or buildings i~~wa~~s often identified as ISA, due to the issue of mixed pixels (Gong et al., 2020b). From this perspective, the results of GISA-10m ~~seem~~ appear more reliable, due to its higher spatial resolution. For instance, in the case of Johannesburg and Los Angeles (Fig. ~~12c~~ 11c and ~~&~~d), GAIA and GAUD exhibit~~ed~~ false alarms in both residential and industrial areas, but these errors a~~we~~re significantly reduced in GISA-10m, due to the superior~~better~~ discriminative~~on~~ ability of the 10-m Sentinel data.

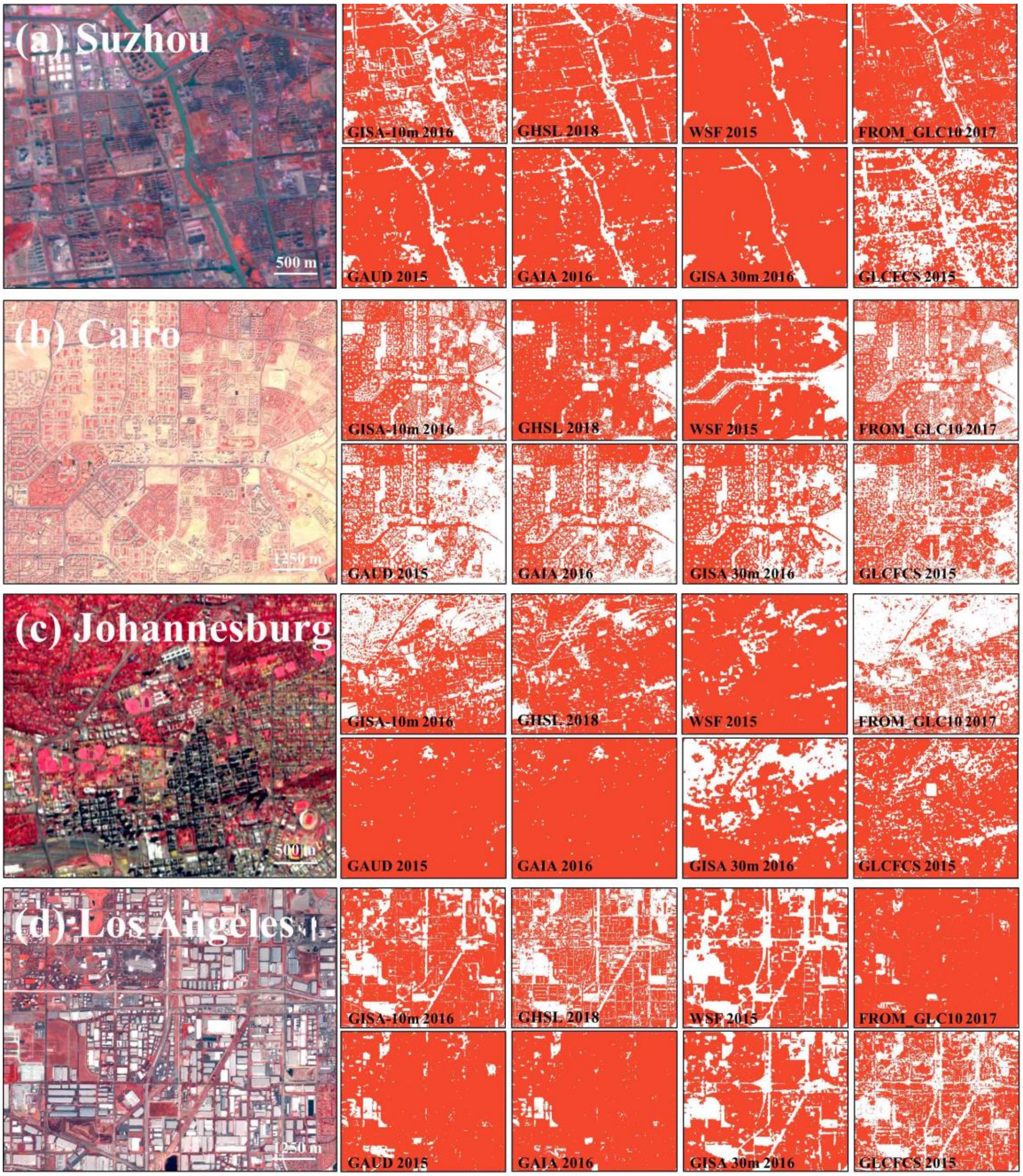

Figure ~~12~~11. Comparison between~~of~~ ~~the~~ GISA-10m and the seven datasets over urban regions in: (a) Suzhou, China; (b) Cairo, Egypt; (c) Johannesburg, South Africa; (d) Los Angeles, US~~the United States~~. The Sentinel-2 images were composited in a~~the~~ false-color combination (R: NIR, G: r~~R~~ed, B: g~~G~~reen).

On the other hand, the agreement between GISA-10m and the existing datasets i~~wa~~s slightly lower in rural regions ($0.5099 < R^2 < 0.6525$). The fitted slopes between the three 30-m datasets (i.e., GISA, GAIA, GAUD) and GISA-10m in the rural regions a~~we~~re all less than one. This phenomenon can be attributed to the finer spatial resolution of GISA-10m, which detects~~ed~~ more rural ISA than the 30-m datasets (Fig~~s~~. ~~13b~~ 12b and ~~&~~d). As for~~to~~ GLCFCS and WSF2015, they possess~~ed~~ more rural ISA than GISA-10m (Fig. ~~11i~~ 10i and ~~&~~k), which could~~may~~ be attributed to their overestimation~~s~~. For example, in Fig~~s~~. ~~13a~~ 12a and ~~&~~c, GLCFCS and WSF2015 fail~~ed~~ to identify the vegetation in the village. FROM_GLC10 ~~seemed~~ appears more consistent with GISA-10m (see the sample from the~~of~~ US in~~,~~ Fig. ~~13d~~12d), but it tends~~ed~~ to underestimate the rural ISA (see Fig~~s~~. ~~13a~~12a –~~-~~c). GHSL_2018 and GISA-10m show~~ed~~ high agreement in ~~the~~ rural regions. However, GHSL_2018 is aimed at~~to~~ outlining~~e~~ human settlements, while GISA-10m is focused on artificial ISA (including buildings, parking lots, roads).

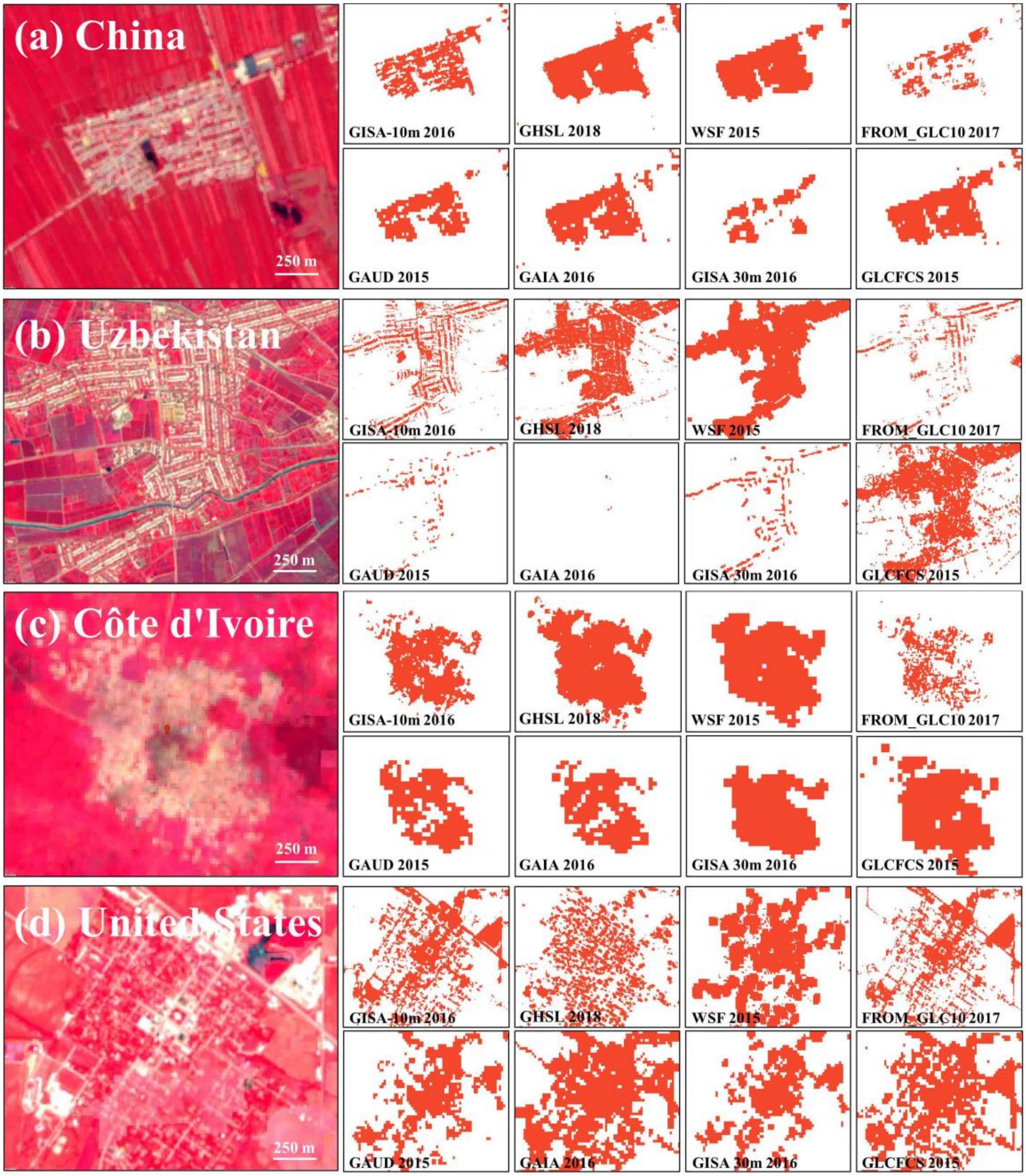

Figure ~~13~~12. Comparison ~~of the~~between GISA-10m and the seven datasets over rural regions in: (a) China (126.348044° E, 45.269079° N);~~,~~ (b) Uzbekistan (60.573313° E, 41.461425° N);~~,~~ (c) Côte d’~~'~~Ivoire (5.853317° W, 6.820244° N);~~,~~ (d) the US~~nited States~~ (90.210747° W, 39.950221° N). The illustration is of Sentinel-2 images with a false-color combination (R: NIR, G: r~~R~~ed, B: g~~G~~reen) to enhance the ISA.

The differences between GHSL_2018, WSF2015, and GISA-10m were further ~~analysed~~analyzed by taking Beijing and Washington as examples. In Fig. ~~14~~13, the overlapping parts between these datasets a~~we~~re marked in different colors, and the regions where the three datasets all agree~~d~~ a~~we~~re shown in gray. In both examples, WSF2015 and ~~GHSL2018~~GHSL_2018 tend~~ed~~ to overestimate the ISA extent (Fig. ~~14b~~13b), and~~.~~ t~~T~~hey wrongly identif y~~ied~~ vegetation as ISA in the low-density residential areas (Fig. ~~14h~~13h). In particular, ~~GHSL2018~~GHSL 2018 successfully detects the~~ed~~ roads in Beijing, but fails~~ed~~ in Washington (see the ~~color of~~ purple color in Fig. ~~14~~13). This may be related to the fact that ~~GHSL2018~~GHSL 2018 uses~~d~~ different sources of training samples in different regions (Corbane et al., 2021). Although WSF2015 generally obtains~~ed~~ similar results to~~with~~ GISA-10m, its detected roads may stem from the overestimation of building boundaries. For instance, WSF2015 ignores~~d~~ the airport runways in the example of Beijing (Fig. ~~14d~~13d). In the case of Washington, WSF2015 i~~wa~~s less capable of delineating scattered buildings than GISA-10m and ~~GHSL2018~~GHSL 2018 (Fig. ~~14f~~13f), possibly because it also incorporates~~d~~ the 30-m Landsat data in the ISA detection. It should be mentioned that ~~GHSL2018~~GHSL 2018 estimates~~d~~ the probability of human settlement, and hence~~,~~ different thresholds could yield different results. Small thresholds a~~we~~re suitable for capturing scattered settlements, but could result in false alarms. In this study, we chose 0.2 as the threshold, as suggested by Corbane et al.~~,~~ (2021).

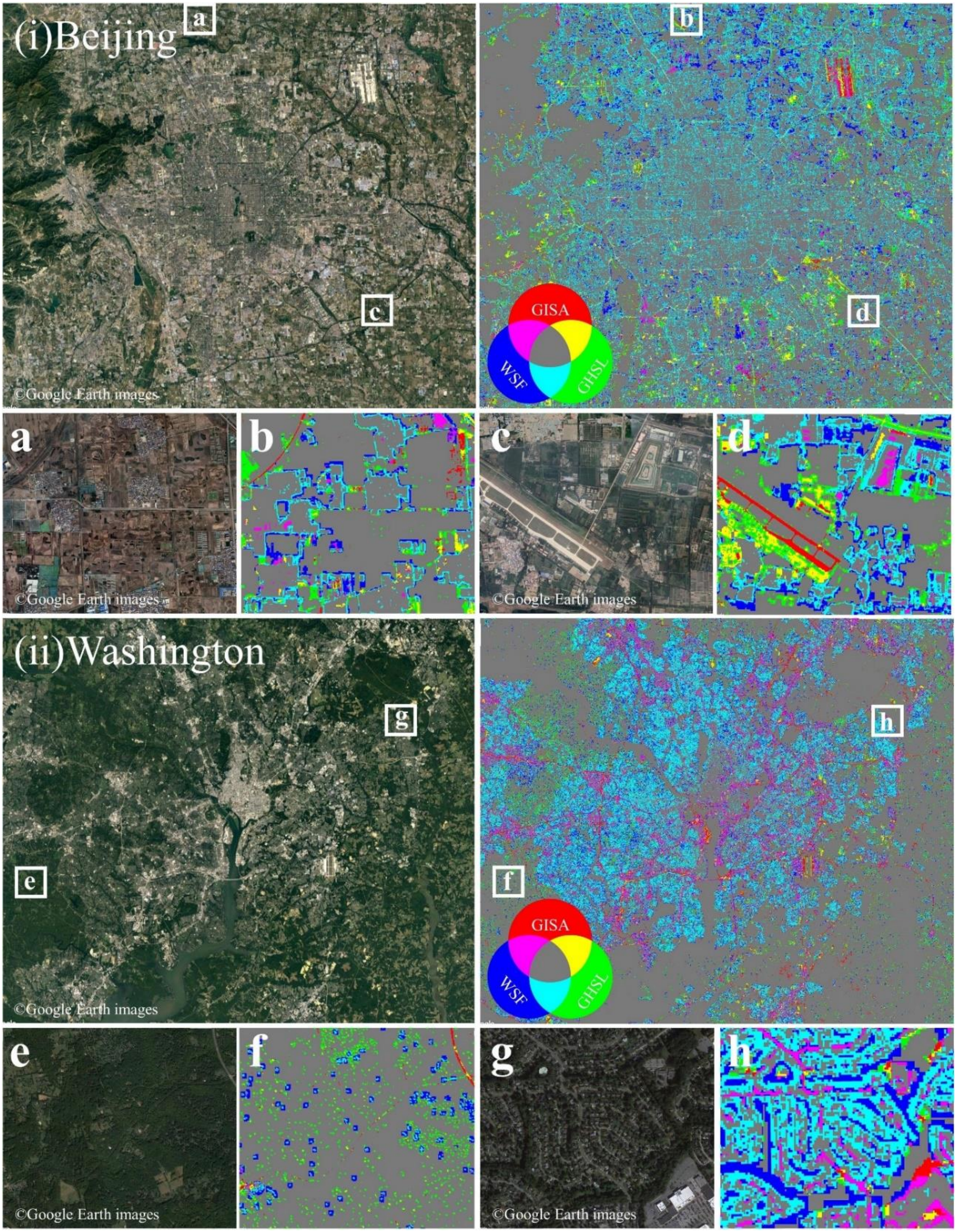

Figure ~~14~~13. I~~The i~~llustration of WSF2015, ~~GHSL2018~~GHSL 2018, and GISA-10m in (i) Beijing and (ii) Washington. Regions where the three datasets all agree~~d~~ a~~we~~re shown in gray.

5.2 Importance of multi-source features

In this study~~paper~~, we ~~proposed~~developed a global ISA mapping method that incorporates~~d~~ spectral, SAR, and temporal information extracted from multi-source Sentinel data. To illustrate the importance of multi-source features in ~~the~~ global ISA mapping, we selected 30 hexagons in terms of the global urban ecoregions (Schneider et al., 2010). Urban ecoregions a~~we~~re defined with reference to biomes, urban landscapes, and economic levels. In each ecoregion, we randomly selected two grid cells~~s~~, with a~~their~~ population of greater or less than 5 million, respectively (Fig. S1). The “~~"~~snow and ice”~~"~~ ecoregion was not considered. Feature contribution estimated by the RF classifier was employed to analyze the relative importance of the multi-source features (Pflugmacher et al., 2014). The d~~D~~ifferent color schemes in Fig. ~~15~~ 14 indicate~~d~~ the different types of features. For instance, the ~~color of~~ blue denotes~~d~~ SAR features while the green represents~~ed~~ the spectral indices. The results indicate~~d~~ that the feature importance varies~~d~~ in the different regions. For example, SAR features a~~we~~re more effective in the temperate grassland of the Middle East and Asia (53N_75E and 50N_39E), while phenological features have~~d~~ more influence in the deciduous forest of Siberia (65N_125E). In particular, SAR features play~~ed~~ a more important role in the more populated regions, e.g., in the temperate forest of North America and Europe as well as the temperate grassland of the Middle East and Asia (Fig. ~~15~~14).

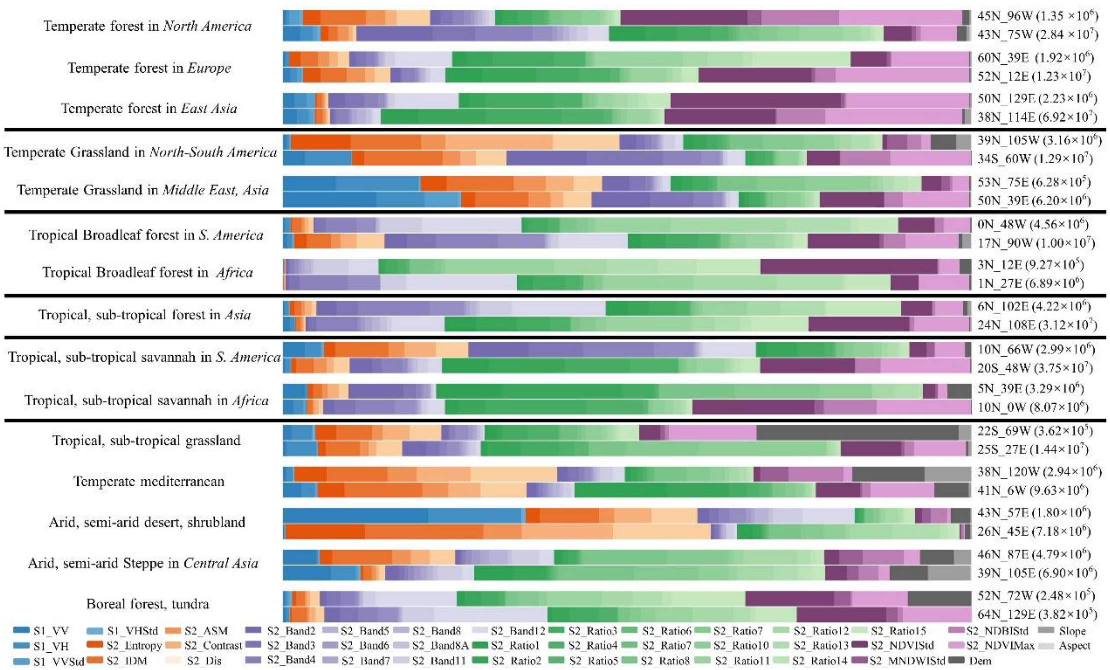

Figure ~~15~~14. Relative importance ~~of~~of the ~~-~~multi-source features in ~~the~~ 30 randomly selected grids located in different urban ecoregions. The labels on the right denote the grid ID and total population. ~~The~~ Dis, IDM, and ASM represents the dissimilarity, angular second moment, and inverse difference moment, respectively.

It is worth noting that although high-rise ISA (e.g., buildings) tends~~ed~~ to have higher radar backscatter~~s~~, the importance of the SAR features i~~wa~~s not always the highest. For example, in the hexagon of central US (45N_96W), the SAR features play~~ed~~ a less significant role than the ~~-~~temporal metrics. In contrast, the spectral indices and phenological information a~~we~~re more effective in this region. For example, as shown in Fig. ~~S4~~ S5 (red squares), in the residential area, the buildings a~~we~~re often surrounded by dense shrubs, which can~~may~~ ~~shrink~~reduce the double bounce scattering. Therefore, the spectral and phenological features have a~~d~~ higher importance since they can better distinguish vegetation from non-vegetation. A similar situation occurs~~red~~ in a desert area (26N_45E), where the SAR features can~~ould~~ not distinguish ISA from NISA effectively, due to the complex topography~~ of mountains~~. In this case, the spectral indices and textures a~~we~~re more effective (Fig. ~~15~~14). However, SAR features a~~we~~re still very important for global ISA mapping, especially for identifying rural buildings (Zhang et al., 2020). Therefore, in this study, we used multi-source features and hexagon-based adaptive RF~~random forest~~ models to ensure that the most suitable features were chosen for the different regions.

5.3 Impact of the training sample size and tree number

Based on the afore-mentioned~~mentioned~~ randomly selected 30 hexagons in different urban ecoregions, we investigated the relationship between the training sample size and the accuracy (Fig. S1). For each hexagon, we fixed the number of NISA samples to 30,000 and changed the number of ISA$_{RS}$ and ISA$_{OSM}$ samples. Specifically, we first randomly selected 1,000 ISA$_{RS}$, 1,000 ISA$_{OSM}$~~-~~, and 2,000 NISA samples from the candidate pool (see Section 3.1.1) as the test samples and used the remaining ones for the training. We randomly selected 50 ISA$_{RS}$ and 50 ISA$_{OSM}$ samples as the initial training samples~~,~~ and, subsequently, in an iterative manner, 400 ISA$_{RS}$ and ISA$_{OSM}$ samples were randomly selected from the pool and added to the training samples to train the RF classifier. It can be observed that all the hexagons reach~~ed~~ saturation with 2~~,~~500 ISA$_{RS}$ and ISA$_{OSM}$ samples (Fig. ~~S5~~S6). Therefore, in this research, we set the number of ISA$_{RS}$, ISA$_{OSM}$, and NISA samples to 2~~,~~500, 2~~,~~500 and 30,000, respectively.

We also analyzed the effect of the tree number on the accuracy of global ISA mapping, using the 30 afore-mentioned~~mentioned~~ mapping grid cells~~s~~ from global urban ecological regions. The results show~~ed~~ that the OA~~overall accuracy~~ i~~wa~~s low and unstable when~~ile~~ the number of trees i~~wa~~s less than 20 (Fig. ~~S6~~S7). As the number of trees increases~~d~~, the mapping accuracy increases~~d~~ and then stabilizes~~d~~ around 200 trees. Therefore, we used 200 trees for each RF~~random forest~~ model in GISA-10m.

5.4 Advantages of locally adaptive RF classification

We used two hexagons located in China (CHN) and Saudi Arabia (SA) to demonstrate the advantages of the adaptive RF~~random forest~~ classification. Although China and Saudi Arabia are both located in Asia, their urban landscapes and architectural~~e~~ styles are significantly different, due to their differences in climate, environment, and culture. In this experiment~~section~~, we migrated the training samples from one hexagon to classify the other one. For example, training samples collected in ~~the~~ SA were~~as~~ used to classify the hexagon of China. The accuracy of each hexagon was evaluated by the visually ~~-~~interpreted samples inside it. ~~It was found that~~The results show that the OA decreases~~d~~ by 34% when the SA samples are~~was~~ applied to CHN (written as SA-to-CHN). Similarly, the OA i~~wa~~s substantially reduced by 23% by the transfer of CHN-to-SA. Furthermore, ~~we found that~~the local samples always outperform~~ed~~ the migrated ones (see Table ~~9~~S7), which verifies~~d~~ the necessity of locally ~~and~~ adaptive classification strategies in ~~the~~ global ISA mapping. Furthermore~~Besides~~, a~~the~~ locally adaptive model is more sensitive to the sample quality ~~compared to the~~than a global model (Radoux et al., 2014), which further shows~~ed~~ the necessity and effectiveness of the local classification strategy.

~~Table 9. Results of quantitative accuracy assessment for China (CHN) and Saudi Arabia (SA) based on local and transferred samples. OA denotes the overall accuracy.~~

	~~Saudi Arabia~~				~~China~~			
	~~OA (%)~~	~~Kappa~~	~~F1-score of ISA (%)~~	~~F1-score of NISA (%)~~	~~OA (%)~~	~~Kappa~~	~~F1-score of ISA (%)~~	~~F1-score of NISA (%)~~
~~ISA_SA & NISA_SA~~	**~~93.00~~**	**~~0.8599~~**	**~~92.39~~**	**~~93.95~~**	~~79.50~~	~~0.5915~~	~~77.60~~	~~81.86~~
~~ISA_SA & NISA_CN~~	~~53.00~~	~~0.7253~~	~~65.44~~	~~26.77~~	~~55.00~~	~~0.5233~~	~~4.35~~	~~70.59~~
~~ISA_CN & NISA_SA~~	~~70.50~~	~~0.8396~~	~~53.23~~	~~78.55~~	~~48.00~~	~~0.6251~~	~~63.38~~	~~10.53~~
~~ISA_CN & NISA_CN~~	~~50.50~~	~~0.0846~~	~~64.77~~	~~16.95~~	**~~89.00~~**	**~~0.7778~~**	**~~86.90~~**	**~~91.30~~**

5.5 Influence of the sources of training samples

In this section, the effects of the training sample sources, i.e., ~~from~~ the remote sensing dataset (ISA$_{RS}$) and the OSM database (ISA$_{OSM}$), were investigated. Various combinations of the ISA$_{RS}$ and ISA$_{OSM}$ training samples were tested at the global scale using the visually ~~-~~interpreted samples from Section 3.2 (Table ~~10~~S8). In general, it can be found that using both sources yields~~ed~~ the most accurate results, which shows~~ed~~ the effectiveness and necessity of ~~incorporati~~incorporating ~~on of~~ training samples from both remote sensing and crowdsourced~~ing~~ OSM data. By further checking the UA and PA of ISA, ~~one~~ it can be seen that using both sample sources significantly improves~~d~~ the PA and reduces~~d~~ the ISA omissions, since the combination of ISA$_{RS}$ and ISA$_{OSM}$ strengthens~~ed~~ the diversity of the training samples. Similarly, it is~~was~~ also found that the multi-source samples significantly raise~~d~~ the PA of NISA and lower~~ed~~ its commission error.

~~Table 10. Results of global accuracy assessment for ISA$_{RS}$ and ISA$_{OSM}$ sample. OA denotes the overall accuracy, while PA and UA indicate the user's accuracy and the producer's accuracy, respectively.~~

~~Source of training sample~~	~~OA (%)~~	~~Kappa~~	~~F1-score of ISA (%)~~	~~F1-score of NISA (%)~~	~~UA of ISA (%)~~	~~PA of ISA (%)~~	~~UA of NISA (%)~~	~~PA of NISA (%)~~
~~NISA+ISA$_{RS}$+ISA$_{OSM}$~~	**~~86.06~~**	**~~0.7165~~**	**~~83.65~~**	**~~88.55~~**	~~86.13~~	**~~81.30~~**	**~~86.01~~**	~~91.25~~
~~NISA+ISA$_{RS}$~~	~~80.24~~	~~0.5871~~	~~73.85~~	~~84.63~~	**~~88.16~~**	~~63.54~~	~~76.73~~	**~~94.35~~**
~~NISA+ISA$_{OSM}$~~	~~82.99~~	~~0.6500~~	~~78.96~~	~~86.34~~	~~86.24~~	~~72.81~~	~~81.17~~	~~92.23~~

Given that geographic bias in the spatial distribution of OSM data can ~~may~~ affect the mapping results (Zacharopoulou et al., 2021), we applied temporal and spatial rules to mitigate the effect of the difference of the spatial distribution. In addition, a spectral rule was used to remove potential errors in the OSM-derived training samples (i.e., ISA$_{OSM}$). In fact, more than 82% of the OSM ways are buildings and highways, whose total number exceeds 700 million (https://taginfo.openstreetmap.org/keys, last accessed: 20 June 2022). Therefore, OSM data provides a reference for large-scale ISA mapping, but have~~it has~~ rarely been employed in global ISA mapping. We calculated the OA~~overall accuracy~~ for the test grid cells~~s~~ where the number of ISA$_{OSM}$ training samples was~~ere~~ less than or larger than 2500 (i.e., the recommended size of training sample in Section 5.3).

The results show~~ed~~ that the accuracy of these regions i~~wa~~s similar to the global accuracy (Table ~~11~~S9). This phenomenon demonstrates~~d~~ the stable performance of GISA-10m. Moreover, global ISA mapping using only ISA_{OSM} training samples shows a~~ed~~ relatively stable accuracy across the continents (Fig. ~~S7~~S8), suggesting that the refined OSM buildings and roads can reduce the impact of their uneven spatial distribution. This can be attributed to the rule-based method we implemented that improved the reliability and spatial consistency of ISA_{OSM}. In addition, the collaboration of ISA_{OSM} improves~~d~~ the OA~~overall accuracy~~ of global ISA mapping by 3% (Table ~~10~~S8), indicating the feasibility of OSM data in enhancing the performance of global ISA mapping, after a series~~t~~ of refinements. Overall, although the spatial distribution of the OSM data is uneven, we tried to balance its spatial distribution through a series of rules, and incorporated multi-source geospatial data (e.g., satellite-derived datasets) to reduce the impact of geographical bias on GISA-10m.

~~**Table 11. Results of quantitative accuracy assessment for test grids with the number of ISA_{OSM} training samples less or more than the recommended size. OA represents the overall accuracy.**~~

~~Type of test grids~~	~~OA (%)~~	~~Kappa~~	~~F1-score of ISA (%)~~	~~F1-score of NISA (%)~~
~~#ISA_{OSM} < 2500~~	~~85.61~~	~~0.7021~~	~~81.79~~	~~89.01~~
~~#ISA_{OSM} > 2500~~	~~86.23~~	~~0.7218~~	~~84.32~~	~~88.35~~
~~All of the above~~	~~86.06~~	~~0.7165~~	~~83.65~~	~~88.55~~

6 Data availability

The GISA-10m dataset~~product~~ generated in this study is available in the public domain at http://doi.org/10.5281/zenodo.5791855 (Huang et al, 2021). The Sentinel data were acquired from the GEE (available at code.earthengine.google.com, last accessed: ~~6~~ August 6, 2021). The GHSL data were~~as~~ provided by the Joint Research Centre at the European Commission (available at https://ghsl.jrc.ec.europa.eu/datasets.php, last accessed: ~~19~~ December 19, 2021). WSF was provided by the German Aerospace Center (https://doi.org/10.6084/m9.figshare.c.4712852, Marconcini et al., 2020).The GlobeLand30 and GAUD were downloaded from the websites of the National Geomatics Center of China (available at http://www.globallandcover.com/, last accessed: ~~6~~ August 6, 2021) and Sun Yat-sen University (available at https://doi.org/10.6084/m9.figshare.11513178.v1, Liu et al., 2020b). The FROM_GLC10, global urban boundaries, and GAIA were ~~assessed from the~~provided by Tsinghua University (available at http://data.ess.tsinghua.edu.cn, last accessed: ~~6~~ August 6, 2021). The GISA was provided by the Institute of Remote Sensing Information Processing at Wuhan University (available at https://zenodo.org/record/5136330, Huang et al., 2021a). The GLCFCS was provided by the Aerospace Information Research Institute at the Chinese Academy of Sciences (available at https://zenodo.org/record/4280923, Zhang et al., 2021). The P~~p~~lanet files were download from the ~~website of~~ OpenStreetMap website (available at https://planet.openstreetmap.org, last accessed: ~~19~~ December 19, 2021).

7 Conclusion

In this study, we proposed a global ISA mapping method and produced a~~the~~ 10-m global ISA dataset (GISA-10m). To the best of our knowledge, this is the first global 10-m resolution ISA dataset~~map~~ based on ~~Sentienl~~Sentinel-1 and 2 data. To this end, a global training sample generation method was ~~proposed~~ introduced based on a series of temporal, spatial, spectral, and geometrical rules, and 58 million training samples were generated from the existing global ISA datasets and ~~the social sensing~~VGI data (i.e., OSM). On the basis of the 2.7 million Sentinel images available o~~i~~n the GEE platform~~oogle Earth Engine (GEE)~~, multi-source features were constructed, including spectral, textural~~e~~, SAR, and temporal metrics. The global terrestrial surface was divided with hexagons, and the results were obtained by a series of RF classifiers. In particular, the mapping was conducted adaptively for each hexagon, by considering the difficulty and diversity for the global ISA detection. The OA~~overall accuracy~~ of GISA-10m exceeded 86%, based on a set of independent test samples. The inter-comparison between the different global ISA datasets ~~showed~~ confirmed the superiority of the~~our~~ results obtained in this study. Based on the GISA-10m dataset, the ISA distribution at the global, continental, and country levels was ~~discussed~~ investigated and compared. In addition, the global ISA distribution was compared between rural and urban areas. In particular, for the first time, ~~by~~ courtesy of the high spatial resolution, the global road ISA was further identified and its distribution was discussed.

The GISA-10m dataset could~~an~~ be used for global climate change studies and urban planning. The~~Our~~ proposed rule-based sample generation method could~~an~~ also be applied for the global mapping of other land~~-~~cover categories. For example, the millions of cropland and forest tags in the OSM database could~~an~~ facilitate global high-resolution cropland and forest mapping. The ISA mapping method via multi-source geospatial data presented in this paper could~~an~~ also be improved by incorporating additional data sources, such as building footprints from Microsoft and Facebook (Corbane et al., 2021). In the future, we plan to extend the temporal coverage of GISA-10m and reveal the global ISA dynamics at the 10-m resolution.

Author contributions. XH conceived the study. XH, JY, WW, and ZL designed and implemented the methodology. JY prepared the original draft and XH revised the manuscript.

Competing interests. The authors declare that they have no conflicts of interest.

Financial support. This research was supported by the National Natural Science Foundation of China (under Grant 41971295), the Special Fund of Hubei Luojia Laboratory (under Grant 220100031), and the Foundation for Innovative Research Groups of the Natural Science Foundation of Hubei Province (under Grant 2020CFA003).

Acknowledgments. The authors greatly appreciate the free access to~~of~~ the Sentinel data provided by ~~the~~ ESA, the GlobeLand30 product provided by the National Geomatics Center of China, the FROM_GLC10 product provided by Tsinghua University, and the GISA data provided by Wuhan University. We would also like to thank the Google Earth Engine team for their excellent work in~~to~~ maintaining the planetary-scale geospatial cloud platform, as well as the volunteers around the world that have contributed to the OpenStreetMap database.

References

Bauer, E. and Kohavi, R.: Empirical comparison of voting classification algorithms: bagging, boosting, and variants, Mach. Learn., 36(1), 105–139, doi:10.1023/a:1007515423169, 1999.

Breiman, L.: Random forests, Mach. Learn., 45(1), 5–32, doi:10.1023/A:1010933404324, 2001.

Chen, J., Chen, J., Liao, A., Cao, X., Chen, L., Chen, X., He, C., Han, G., Peng, S., Lu, M., Zhang, W., Tong, X. and Mills, J.: Global land cover mapping at 30 m resolution: A POK-based operational approach, ISPRS J. Photogramm. Remote Sens., 103, 7–27, doi:10.1016/j.isprsjprs.2014.09.002, 2015.

Clausi, D. A.: An analysis of co-occurrence texture statistics as a function of grey level quantization, Can. J. Remote Sens., 28(1), 45–62, doi:10.5589/m02-004, 2002.

Corbane, C., Syrris, V., Sabo, F., Politis, P., Melchiorri, M., Pesaresi, M., Soille, P. and Kemper, T.: Convolutional neural networks for global human settlements mapping from Sentinel-2 satellite imagery, Neural Comput. Appl., 33(12), 6697–6720, doi:10.1007/s00521-020-05449-7, 2021.

Dewan, A. M. and Yamaguchi, Y.: Land use and land cover change in Greater Dhaka, Bangladesh: Using remote sensing to promote sustainable urbanization, Appl. Geogr., 29(3), 390–401, doi:10.1016/j.apgeog.2008.12.005, 2009.

Drusch, M., Del Bello, U., Carlier, S., Colin, O., Fernandez, V., Gascon, F., Hoersch, B., Isola, C., Laberinti, P., Martimort, P., Meygret, A., Spoto, F., Sy, O., Marchese, F. and Bargellini, P.: Sentinel-2: ESA's Optical High-Resolution Mission for GMES Operational Services, Remote Sens. Environ., 120, 25–36, doi:https://doi.org/10.1016/j.rse.2011.11.026, 2012.

Fonte, C. C., Patriarca, J., Jesus, I. and Duarte, D.: Automatic Extraction and Filtering of OpenStreetMap Data to Generate Training Datasets for Land Use Land Cover Classification, Remote Sens. , 12(20), doi:10.3390/rs12203428, 2020.

Foody, G. M.: Sample size determination for image classification accuracy assessment and comparison, Int. J. Remote Sens., 30(20), 5273–5291, doi:10.1080/01431160903130937, 2009.

Foody, G. M. and Arora, M. K.: An evaluation of some factors affecting the accuracy of classification by an artificial neural network, Int. J. Remote Sens., 18(4), 799–810, doi:10.1080/014311697218764, 1997.

Friedl, M. A., Sulla-Menashe, D., Tan, B., Schneider, A., Ramankutty, N., Sibley, A. and Huang, X.: MODIS Collection 5 global land cover: Algorithm refinements and characterization of new datasets, Remote Sens. Environ., 114(1), doi:10.1016/j.rse.2009.08.016, 2010.

Gamba, P. and Lisini, G.: Fast and Efficient Urban Extent Extraction Using ASAR Wide Swath Mode Data, IEEE J. Sel. Top. Appl. Earth Obs. Remote Sens., 6(5), 2184–2195, doi:10.1109/JSTARS.2012.2235410, 2013.

Goetz, M.: Towards generating highly detailed 3D CityGML models from OpenStreetMap, Int. J. Geogr. Inf. Sci., 27(5), 845–865, doi:10.1080/13658816.2012.721552, 2013.

Goetz, S. J., Wright, R. K., Smith, A. J., Zinecker, E. and Schaub, E.: IKONOS imagery for resource management: Tree cover, impervious surfaces, and riparian buffer analyses in the mid-Atlantic region, Remote Sens. Environ., 88(1–2), 195–208, doi:10.1016/j.rse.2003.07.010, 2003.

Goldblatt, R., You, W., Hanson, G. and Khandelwal, A. K.: Detecting the Boundaries of Urban Areas in India: A Dataset for Pixel-Based Image Classification in Google Earth Engine, Remote Sens. , 8(8), doi:10.3390/rs8080634, 2016.

Goldblatt, R., Stuhlmacher, M. F., Tellman, B., Clinton, N., Hanson, G., Georgescu, M., Wang, C., Serrano-Candela, F., Khandelwal, A. K., Cheng, W.-H. and Balling, R. C.: Using Landsat and nighttime lights for supervised pixel-based image classification of urban land cover, Remote Sens. Environ., 205, 253–275, doi:https://doi.org/10.1016/j.rse.2017.11.026, 2018.

Gong, J., Liu, C. and Huang, X.: Advances in urban information extraction from high-resolution remote sensing imagery, Sci. China Earth Sci., 63(4), 463–475, doi:10.1007/s11430-019-9547-x, 2020a.

Gong, P., Liu, H., Zhang, M., Li, C., Wang, J., Huang, H., Clinton, N., Ji, L., Li, W., Bai, Y., Chen, B., Xu, B., Zhu, Z., Yuan, C., Ping Suen, H., Guo, J., Xu, N., Li, W., Zhao, Y., Yang, J., Yu, C., Wang, X., Fu, H., Yu, L., Dronova, I., Hui, F., Cheng, X., Shi, X., Xiao, F., Liu, Q. and Song, L.: Stable classification with limited sample: transferring a 30-m resolution sample set collected in 2015 to mapping 10-m resolution global land cover in 2017, Sci. Bull., 64(6), 370–373, doi:10.1016/j.scib.2019.03.002, 2019.

Gong, P., Li, X., Wang, J., Bai, Y., Chen, B., Hu, T., Liu, X., Xu, B., Yang, J., Zhang, W. and Zhou, Y.: Annual maps of global artificial impervious area (GAIA) between 1985 and 2018, Remote Sens. Environ., 236, 111510, doi:10.1016/j.rse.2019.111510, 2020b.

Goodchild, M. F.: Citizens as sensors: the world of volunteered geography, GeoJournal, 69(4), 211–221, doi:10.1007/s10708-007-9111-y, 2007.

Gorelick, N., Hancher, M., Dixon, M., Ilyushchenko, S., Thau, D. and Moore, R.: Google Earth Engine: Planetary-scale geospatial analysis for everyone, Remote Sens. Environ., 202, 18–27, doi:10.1016/j.rse.2017.06.031, 2017.

Haklay, M. and Weber, P.: OpenStreetMap: User-Generated Street Maps, IEEE Pervasive Comput., 7(4), 12–18, doi:10.1109/MPRV.2008.80, 2008.

Herold, M., Latham, J. S., Di Gregorio, A. and Schmullius, C. C.: Evolving standards in land cover characterization, J. Land Use Sci., 1(2–4), 157–168, doi:10.1080/17474230601079316, 2006.

Huang, X. and Zhang, L.: An SVM Ensemble Approach Combining Spectral, Structural, and Semantic Features for the Classification of High-Resolution Remotely Sensed Imagery, IEEE Trans. Geosci. Remote Sens., 51(1), 257–272, doi:10.1109/TGRS.2012.2202912, 2013.

Huang, X., Li, J., Yang, J., Zhang, Z., Li, D., Liu, X., Xin, H., Jiayi, L., Jie, Y., Zhen, Z., Dongrui, L. and Xiaoping, L.: 30 m global impervious surface area dynamics and urban expansion pattern observed by Landsat satellites: From 1972 to 2019, Sci. CHINA Earth Sci., doi:10.1007/s11430-020-9797-9, 2021.

Huang, X., Song, Y., Yang, J., Wang, W., Ren, H., Dong, M., Feng, Y., Yin, H. and Li, J.: Toward accurate mapping of 30-m time-series global impervious surface area (GISA), Int. J. Appl. Earth Obs. Geoinf., 109, 102787, doi:https://doi.org/10.1016/j.jag.2022.102787, 2022.

Ji, H., Li, X., Wei, X., Liu, W., Zhang, L. and Wang, L.: Mapping 10-m Resolution Rural Settlements Using Multi-Source Remote Sensing Datasets with the Google Earth Engine Platform, Remote Sens. , 12(17), doi:10.3390/rs12172832, 2020.

Li, X., Gong, P., Zhou, Y., Wang, J., Bai, Y., Chen, B., Hu, T., Xiao, Y., Xu, B., Yang, J., Liu, X., Cai, W., Huang, H., Wu, T., Wang, X., Lin, P., Li, X., Chen, J., He, C., Li, X., Yu, L., Clinton, N. and Zhu, Z.: Mapping global urban boundaries from the global artificial impervious area (GAIA) data, Environ. Res. Lett., 15(9), 94044, doi:10.1088/1748-9326/ab9be3, 2020.

Lin, Y., Zhang, H., Lin, H., Gamba, P. E. and Liu, X.: Incorporating synthetic aperture radar and optical images to investigate the annual dynamics of anthropogenic impervious surface at large scale, Remote Sens. Environ., 242, 111757, doi:https://doi.org/10.1016/j.rse.2020.111757, 2020.

Liu, C., Huang, X., Zhu, Z., Chen, H., Tang, X. and Gong, J.: Automatic extraction of built-up area from ZY3 multi-view satellite imagery: Analysis of 45 global cities, Remote Sens. Environ., 226, 51–73, doi:https://doi.org/10.1016/j.rse.2019.03.033, 2019.

Liu, D., Chen, N., Zhang, X., Wang, C. and Du, W.: Annual large-scale urban land mapping based on Landsat time series in Google Earth Engine and OpenStreetMap data: A case study in the middle Yangtze River basin, ISPRS J. Photogramm. Remote Sens., 159, 337–351, doi:https://doi.org/10.1016/j.isprsjprs.2019.11.021, 2020a.

Liu, H., Gong, P., Wang, J., Clinton, N., Bai, Y. and Liang, S.: Annual dynamics of global land cover and its long-term changes from 1982 to 2015, Earth Syst. Sci. Data, 12(2), 1217–1243, doi:10.5194/essd-12-1217-2020, 2020b.

Liu, X., Huang, Y., Xu, X., Li, X., Li, X., Ciais, P., Lin, P., Gong, K., Ziegler, A. D., Chen, A., Gong, P., Chen, J., Hu, G., Chen, Y., Wang, S., Wu, Q., Huang, K., Estes, L. and Zeng, Z.: High-spatiotemporal-resolution mapping of global urban change from 1985 to 2015, Nat. Sustain., 3(7), 564–570, doi:10.1038/s41893-020-0521-x, 2020c.

Marconcini, M., Metz-Marconcini, A., Üreyen, S., Palacios-Lopez, D., Hanke, W., Bachofer, F., Zeidler, J., Esch, T., Gorelick, N., Kakarla, A., Paganini, M. and Strano, E.: Outlining where humans live, the World Settlement Footprint 2015, Sci. Data, 7(1), 242, doi:10.1038/s41597-020-00580-5, 2020.

Olofsson, P., Foody, G. M., Herold, M., Stehman, S. V., Woodcock, C. E. and Wulder, M. A.: Good practices for estimating area and assessing accuracy of land change, Remote Sens. Environ., 148, 42–57, doi:10.1016/j.rse.2014.02.015, 2014.

Olson, D. M., Dinerstein, E., Wikramanayake, E. D., Burgess, N. D., Powell, G. V. N., Underwood, E. C., D'Amico, J. A., Itoua, I., Strand, H. E., Morrison, J. C., Loucks, C. J., Allnutt, T. F., Ricketts, T. H., Kura, Y., Lamoreux, J. F., Wettengel,

W. W., Hedao, P. and Kassem, K. R.: Terrestrial ecoregions of the world: A new map of life on Earth, Bioscience, 51(11), 933–938, doi:10.1641/0006-3568(2001)051[0933:TEOTWA]2.0.CO;2, 2001.

Pflugmacher, D., Cohen, W. B., Kennedy, R. E. and Yang, Z.: Using Landsat-derived disturbance and recovery history and lidar to map forest biomass dynamics, Remote Sens. Environ., 151, 124–137, doi:https://doi.org/10.1016/j.rse.2013.05.033, 2014.

Puissant, A., Hirsch, J. and Weber, C.: The utility of texture analysis to improve per-pixel classification for high to very high spatial resolution imagery, Int. J. Remote Sens., 26(4), 733–745, doi:10.1080/01431160512331316838, 2005.

Qin, L., Wu, W., Tian, Y. and Xu, W.: LiDAR Filtering of Urban Areas With Region Growing Based on Moving-Window Weighted Iterative Least-Squares Fitting, IEEE Geosci. Remote Sens. Lett., 14(6), 841–845, doi:10.1109/LGRS.2017.2682854, 2017.

Qin, L., Xu, W., Tian, Y., Chen, B. and Wang, S.: A River Channel Extraction Method for Urban Environments Based on Terrain Transition Lines, Water Resour. Res., 54(7), 4887–4900, doi:https://doi.org/10.1029/2018WR023095, 2018.

Radoux, J., Lamarche, C., Van Bogaert, E., Bontemps, S., Brockmann, C. and Defourny, P.: Automated training sample extraction for global land cover mapping, Remote Sens., 6(5), 3965–3987, doi:10.3390/rs6053965, 2014.

Richards, T., Gallego, J. and Achard, F.: Sampling for forest cover change assessment at the pan-tropical scale, Int. J. Remote Sens., 21(6–7), 1473–1490, doi:10.1080/014311600210272, 2000.

Rodriguez-Galiano, V. F., Chica-Olmo, M., Abarca-Hernandez, F., Atkinson, P. M. and Jeganathan, C.: Random Forest classification of Mediterranean land cover using multi-seasonal imagery and multi-seasonal texture, Remote Sens. Environ., 121, 93–107, doi:https://doi.org/10.1016/j.rse.2011.12.003, 2012.

Stehman, S. V: Impact of sample size allocation when using stratified random sampling to estimate accuracy and area of land-cover change, Remote Sens. Lett., 3(2), 111–120, doi:10.1080/01431161.2010.541950, 2012.

Stehman, S. V and Foody, G. M.: Key issues in rigorous accuracy assessment of land cover products, Remote Sens. Environ., 231, 111199, doi:https://doi.org/10.1016/j.rse.2019.05.018, 2019.

Tian, Y., Chen, H., Song, Q. and Zheng, K.: A Novel Index for Impervious Surface Area Mapping: Development and Validation, Remote Sens. , 10(10), doi:10.3390/rs10101521, 2018.

Tian, Y., Zhou, Q. and Fu, X.: An Analysis of the Evolution, Completeness and Spatial Patterns of OpenStreetMap Building Data in China, ISPRS Int. J. Geo-Information , 8(1), doi:10.3390/ijgi8010035, 2019.

Tucker, C. J.: Red and photographic infrared linear combinations for monitoring vegetation, Remote Sens. Environ., 8(2), 127–150, doi:10.1016/0034-4257(79)90013-0, 1979.

United Nations: Goal 11: Sustainable Cities and Communities - SDG Tracker, [online] Available from: https://sdg-tracker.org/cities (Accessed 25 April 2021), 2016.

Veloso, A., Mermoz, S., Bouvet, A., Le Toan, T., Planells, M., Dejoux, J.-F. and Ceschia, E.: Understanding the temporal behavior of crops using Sentinel-1 and Sentinel-2-like data for agricultural applications, Remote Sens. Environ., 199, 415–426, doi:https://doi.org/10.1016/j.rse.2017.07.015, 2017.

Voss, P. R.: Demography as a Spatial Social Science, Popul. Res. Policy Rev., 26(5), 457–476, doi:10.1007/s11113-007-9047-4, 2007.

Woodcock, C. E., Allen, R., Anderson, M., Belward, A., Bindschadler, R., Cohen, W., Gao, F., Goward, S. N., Helder, D., Helmer, E., Nemani, R., Oreopoulos, L., Schott, J., Thenkabail, P. S., Vermote, E. F., Vogelmann, J., Wulder, M. A. and Wynne, R.: Free access to landsat imagery, Science (80-.)., 320(5879), 1011, doi:10.1126/science.320.5879.1011a, 2008.

Wulder, M. A., Coops, N. C., Roy, D. P., White, J. C. and Hermosilla, T.: Land cover 2.0, Int. J. Remote Sens., 39(12), 4254–4284, doi:10.1080/01431161.2018.1452075, 2018.

Xu, H.: Modification of normalised difference water index (NDWI) to enhance open water features in remotely sensed imagery, Int. J. Remote Sens., 27(14), 3025–3033, doi:10.1080/01431160600589179, 2006.

Yang, J. and Huang, X.: The 30 m annual land cover dataset and its dynamics in China from 1990 to 2019, Earth Syst. Sci. Data, 13(8), 3907–3925, doi:10.5194/essd-13-3907-2021, 2021.

Yang, Q., Huang, X. and Tang, Q.: The footprint of urban heat island effect in 302 Chinese cities: Temporal trends and associated factors, Sci. Total Environ., 655, 652–662, doi:10.1016/j.scitotenv.2018.11.171, 2019.

You, N., Dong, J., Huang, J., Du, G., Zhang, G., He, Y., Yang, T., Di, Y. and Xiao, X.: The 10-m crop type maps in Northeast China during 2017–2019, Sci. Data, 8(1), 41, doi:10.1038/s41597-021-00827-9, 2021.

Zacharopoulou, D., Skopeliti, A. and Nakos, B.: Assessment and Visualization of OSM Consistency for European Cities, ISPRS Int. J. Geo-Information , 10(6), doi:10.3390/ijgi10060361, 2021.

Zha, Y., Gao, J. and Ni, S.: Use of normalized difference built-up index in automatically mapping urban areas from TM imagery, Int. J. Remote Sens., 24(3), 583–594, doi:10.1080/01431160304987, 2003.

Zhang, H. K., Roy, D. P., Yan, L., Li, Z., Huang, H., Vermote, E., Skakun, S. and Roger, J.-C.: Characterization of Sentinel-2A and Landsat-8 top of atmosphere, surface, and nadir BRDF adjusted reflectance and NDVI differences, Remote Sens. Environ., 215, 482–494, doi:https://doi.org/10.1016/j.rse.2018.04.031, 2018.

Zhang, X., Liu, L., Wu, C., Chen, X., Gao, Y., Xie, S. and Zhang, B.: Development of a global 30m impervious surface map using multisource and multitemporal remote sensing datasets with the Google Earth Engine platform, Earth Syst. Sci. Data, 12(3), 1625–1648, doi:10.5194/essd-12-1625-2020, 2020.

Zhang, Y., Zhang, H. and Lin, H.: Improving the impervious surface estimation with combined use of optical and SAR remote sensing images, Remote Sens. Environ., 141, 155–167, doi:https://doi.org/10.1016/j.rse.2013.10.028, 2014.